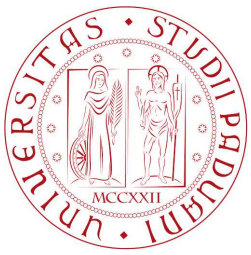

UNIVERSITÀ DEGLI STUDI DI PADOVA

Dipartimento di Fisica e Astronomia "Galileo Galilei"

Master Degree in Physics

Final Dissertation

Investigation of intrinsic error fields in MAST-U device (Oxford, UK)

Thesis supervisor

Dr. Lidia Piron

Candidate

Matteo Gambrioli

Academic Year 2021/2022

Abstract

In magnetic fusion devices, undesired non-axisymmetric magnetic field perturbations, typically called error fields, have been observed to have a detrimental effect on plasma stability and confinement. These spurious perturbations can arise from many sources, namely misalignment introduced in the construction of the device, imperfections in the manufacture of the field coils, 3D structures in the wall surrounding the plasma, current feeds and the presence of ferromagnetic materials near the plasma surface [1] [2].

Error fields with toroidal mode number $n = 1$ can destabilize magnetic islands in otherwise tearing-stable plasmas, as the m=2, n=1 mode (being m the poloidal mode number), leading to plasma termination. Moreover, error fields can inhibit the exploration of some operational regimes, such as at low density and at high-pressure, and within a plasma scenario, they can be also responsible of fast ion losses, rotation braking, thus causing plasma performance degradation.

The main strategies that can be adopted to reduce n=1 error fields are: a careful alignment of the divertor, poloidal field coils, i.e. applying coil shift and tilt, when assembling a fusion device [1], and the installation of error field correction coils capable of inducing a magnetic field pattern which counteract the error field source [3].

In this Thesis work, a database of 90 discharges performed in the MAST-U device, upgrade of the previous MAST tokamak, located at the Culham Centre for Fusion Energy, Oxfordshire, England, has been analyzed to achieve the following objectives: i) identify the n=1 error field and ii) investigate the dependence of the m=2, n=1 mode onset, i.e. the locked mode, with plasma density.

During the assembly of MAST-U, to minimize the n=1 intrinsic error field due to the coil manufacturing, a careful alignment of the magnetic field coils has been applied. To assess the presence of a residual error field, the compass scan method has been executed. This method consists in triggering a locked mode by applying a n=1 probing error field with different phases and relies on an accurate detection of the locked mode onset.

In this Thesis work, a robust and reliable tool able to detect such a triggering mechanism has been developed which allows to reach the objectives above mentioned. Thanks to its portability, such a tool can be also exploited for real-time applications, such as disruption avoidance, as proposed in the next MAST-U campaign.

Contents

1 Error fields in magnetically confined fusion plasmas

In this chapter, an introduction to controlled thermonuclear fusion and to the magnetic confinement of hot plasmas is given, motivating the efforts undertaken in this line of research. This overview is complimented with a theoretical background as well as the current exploitation of this technology, the potentiality and main limitations. The chapter ends with the description of error fields, the main causes, consequences and possible strategies to reduce their effect on the plasma performance.

1.1 Principles of thermonuclear fusion

Nuclear fusion is the process in which two light nuclei fuse together forming a heavier nucleus with a subsequent release of energy in the form of kinetic energy of the reaction products.

Considering the binding energy per nucleon reported in Fig.(1), since an increase in binding energy corresponds to energy production, it is apparent that fusion reactions take place in the left part of the plot, i.e. involve light nuclei [4][5][6]. An increase in the binding energy translates in a mass deficit for the fusion products. This mass deficit corresponds to energy according to the formula $E = mc^2$, which is the energy released in fusion processes.

Fusion processes are widely spread in nature. For example, Stars employ fusion in order to sustain their internal temperature [7]. Starting for the 50's, the research on thermonuclear fusion started to grow aiming at recreating in magnetic fusion devices such fusion processes, and exploiting thus a practically inexhaustible and inherently safe source of energy [8][9]. This energy source has also the advantage of not producing either greenhouse gases or long-lived radioactive waste.

The main fusion reactions of interest for energy production in magnetic fusion devices are [10][11]:

$$^2\mathrm{D} + {}^2\mathrm{D} \rightarrow {}^3\mathrm{He} + {}^1\mathrm{n} + 3.27MeV \tag{1}$$

$$^2\mathrm{D} + {}^2\mathrm{D} \rightarrow {}^3\mathrm{T} + {}^1\mathrm{H} + 4.03MeV \tag{2}$$

$$^2\mathrm{D} + {}^3\mathrm{T} \rightarrow {}^4\mathrm{He} + {}^1\mathrm{n} + 17.6MeV \tag{3}$$

$$^2\mathrm{D} + {}^3\mathrm{He} \rightarrow {}^4\mathrm{He} + {}^1\mathrm{H} + 18.3MeV \tag{4}$$

where the D and T stand for two Hydrogen isotopes: Deuterium, formed by one proton and one neutron, and Tritium, formed by one proton and two neutrons.

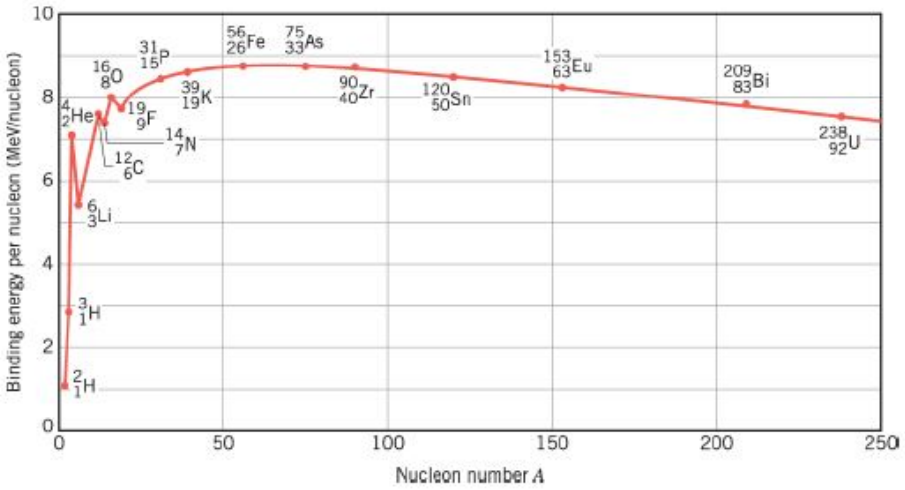

Figure 1: Binding energy per nucleon as a function of the mass number.

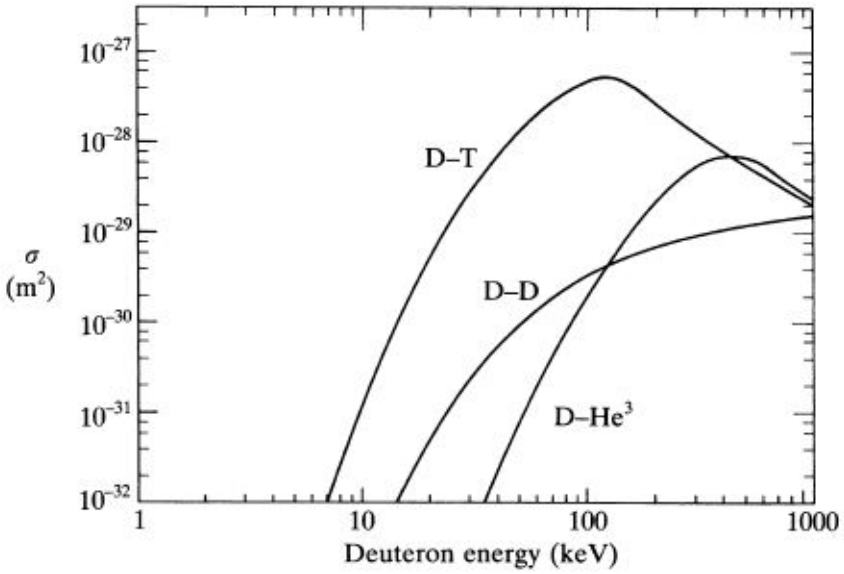

Figure 2: Comparison of cross sections as functions of the deuteron beam energy for reactions D-T [3], D-D [12] and D-He^3 [4] [10] [12].

The fusion reaction cross sections as functions of kinetic energy of the incoming particle (in the reference frame in which the target particle is stationary) is shown in Fig.(2) [10] [12]. Note that the reaction with the highest cross section is the D-T one. For this reason, D-T reaction is most suited to be exploited in a fusion reactor, despite the disadvantages resulting from the fact that T is radioactive and has to be artificially produced because it does not exist in nature, having a half life of 12.3 years only [10].

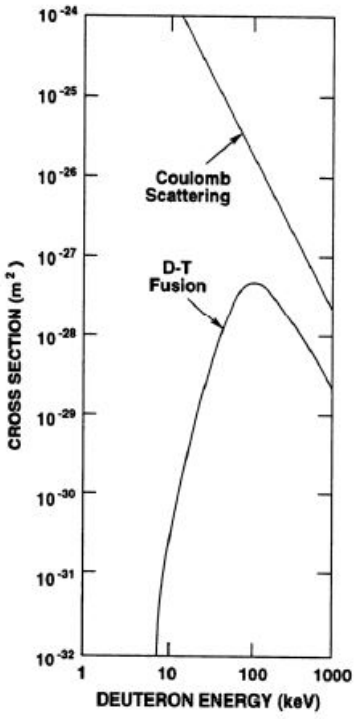

Figure 3: Comparison between elastic Coulomb interaction and fusion interaction for D-T [3] reaction [10] [12].

In a D-T fusion reaction, a nucleus of D and one of T fuse, with the production of an α particle, i.e. Helium nucleus, a neutron and 17.6 MeV of energy. In particular, the released energy is in the form of kinetic energy of the fusion products: the α particle has 3.5 MeV, and the neutron 14.1 MeV.

In principle, the simplest approach to obtain fusion reactions is to accelerate to the required energy a beam of ions of one kind, and send it to a target composed of atoms of the other kind, or collide head-on two beams of the two different ions. However this approach is energetically disadvantageous since the elastic collision cross section is at least two orders of magnitude larger than that for the D-T fusion reactions [10] [12], as can be seen in Fig.(3). This means that in practice more elastic collisions with respect to the fusion processes will occur, losing the energy spent to accelerate these particles. In this way it is impossible to reach a positive energy balance.

Therefore, it is necessary to create a plasma made up of the two ion species and keep it contained in a small volume for a period of time that is significantly longer than the collisional time. In this manner ions can fuse together without losing energy in elastic collisions.

There are mainly two ways to confine a plasma i.e. *magnetic confinement* [13] and *inertial confinement* [14].

- *Magnetic confinement* exploits the fact that charged particles in a magnetic fiel orbit around the magnetic field lines, and are thus confined, on a characteristic space scale equal to the radius of the orbit (Larmor radius), in the plane perpendicular to the field. This is the method on which the European Fusion Programme is based [15] [16].
- *Inertial confinement* uses a target made of solid deuterium and tritium. This target is heated up with high power laser beams, or with heavy ion beams. This causes a vaporization of the external layer and a compression of the inner part, where a strong density increase, allows to overcome the Coulomb barrier and fuse the two species.

Among these two methods to confine a plasma, in this Thesis work, plasmas confined in magnetic fusion devices have been investigated.

1.2 Power Balance

A fusion reactor is a device which induces enough fusion reactions to yield a positive energy balance: in other words, the produced energy, taking into account also the efficiency of conversion in electrical energy, must be sufficiently larger than that required to make it work. Leaving apart the conversion into a electrical energy we can focus on the power balance of the reactor taking into account the gains and the losses. Considering a plasma made up of electrons and ions at the same temperature T, and number density n, the average kinetic energy per particle of each species will be given, according to the kinetic theory of gases, by (3/2)T [10]. The thermal energy density[1] is therefore simply given by:

$$w = 3nT \tag{5}$$

Clearly if temperature gradients are present, as it is usually the case, the quantity nT should be volume averaged. The energy rate equation can be written as follows:

$$\frac{\mathrm{d}w}{\mathrm{d}t} = p_H + p_\alpha - p_L - p_R \tag{6}$$

where p_H is the external heating power density i.e. the energy delivered to the plasma to heat it up. This is done in mainly two ways NBI [17] [18] and radiofrequency heating [19]. The

[1] T is typically expressed in keV in fusion science. 1 eV corresponds to approximately 11600 K.

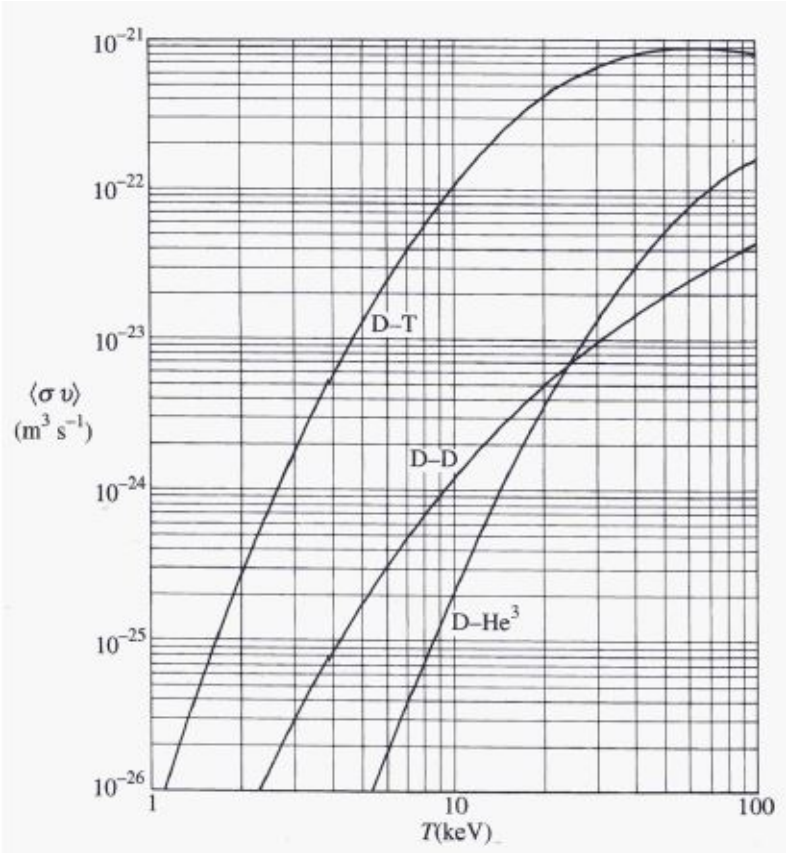

Figure 4: Comparison of the reactivity as function of the temperature for the reactions D-T 3, D-D 12 and D-He^3 4 [10].

first method consists in the injection of energetic neutral particles beams (NBI) which are then ionized inside the plasma and release their energy through subsequent Coulomb collisions i.e. thermalizing. The second method consists into sending electromagnetic waves inside the plasma which then release energy through a particle-wave process called Landau damping [7].

The quantity p_α represents the fraction of the power density produced by the fusion reactions which goes into plasma heating, p_R is the power density lost due the radiation losses i.e. electromagnetic waves coming out from the the plasma while p_L is the power lost through other processes (conduction and convection), usually called power lost by transport processes. In the following, expressions for each quantities aforementioned are provided.

The total power density produced by fusion reactions [10] is given by:

$$p_f = n_D n_T \langle \sigma v \rangle E_f \tag{7}$$

were n_D and n_T are deuterium and tritium number density, E_f is the energy produced by a single fusion reaction and $\langle \sigma v \rangle$ is the reactivity i.e. a physical quantity proportional to the number of fusions reaction occurring for unit time and volume, function of the temperature. Using thermodynamics is possible to give a simplified expression [10], for deuterium and tritium fusion reaction in the 10-20 keV range, of the reactivity:

$$\langle \sigma v \rangle = 1.1 \times 10^{-24} T^2 \quad m^3 s^{-1} \tag{8}$$

In Fig.(4) the reactivity is plotted as a function of the temperature. Note that among the reactions presented, the D-T reaction is the most favorable one. Looking to expression 7 we can easily realize that the best ratio of deuterium and tritium fuel concentration occurs when $n_D = n_T = n/2$. This could be also deduced by looking to the reaction expression 3, which has 1:1 stoichiometry ratio.

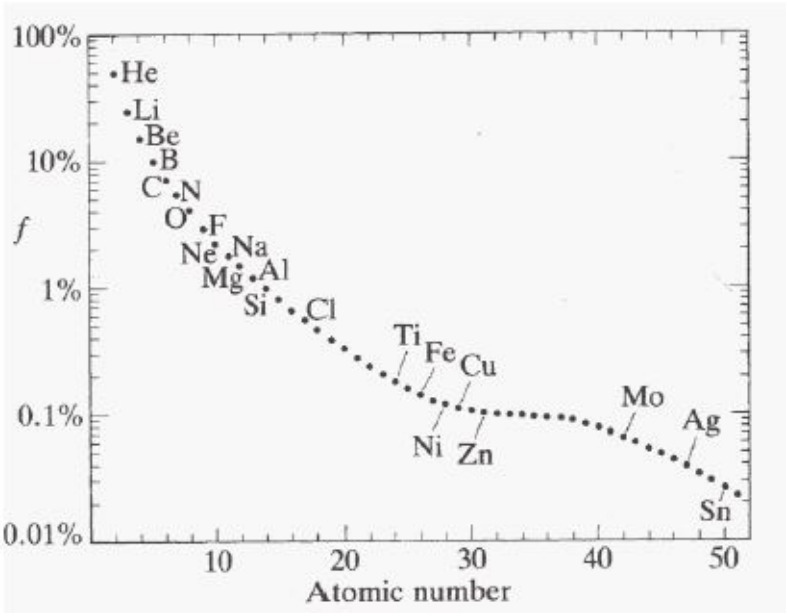

Figure 5: Impurity fraction required to radiate 10% of the fusion power at 10 keV [10].

In presence of D-T fusion reactions, the energy fraction carried by the neutrons exits the plasma and, intercepted by appropriate shields, becomes available for electricity production in the form of thermal energy of a cooling fluid. On the other hand, the α-particles, being charged, remain confined inside the plasma, where they release their energy, 3.5 MeV, to the plasma itself by collisions. It is therefore customary to speak about α-particle heating, with a specific power expressed by this formula:

$$p_\alpha = \frac{1}{4} n^2 \langle \sigma v \rangle E_\alpha \tag{9}$$

The radiated power consists in three contributions: the *bremsstrahlung* radiation due charge particles accelerated and decelerated during Coulomb interaction [20] [21], line radiation due to not-fully ionized atoms whose electrons are first excited by Coulomb interaction and then relax emitting electromagnetic waves [22] and the so called cyclotron radiation, which is linked to the gyration motion of the charged particles around the magnetic field lines. However, this contribution gives a negligible contribution, except at extremely high temperature, since the plasma is opaque at these frequency, and therefore absorbs most of the emitted power [23].

Line radiation is mainly related to impurities inside the plasma. In principle, line radiation could be reduced to zero by having a pure fully ionized plasma. In reality even a small fraction of impurities can severely worsen the power balance. Fig.(5) [10] shows the fraction in impurities required to radiate the 10% of the total fusion power at 10 keV as a function of the atomic number. There are techniques however which go under the name of wall conditioning [24] such as baking, or driving low temperature glow-discharge plasmas inside the device in order to reduce the impurity concentration.

Therefore we can conclude that p_R=p_b with p_b the power density radiated by *bremsstrahlung* which can be estimated as follows:

$$p_b = \alpha_b n^2 T^{1/2} \quad Wm^{-3} \tag{10}$$

with $\alpha_b = 5.35 \times 10^{-37} \quad Wm^3 keV^{1/2}$ [10] [21]. As you can see again we have a square dependence in density. The energy loss rate due to transport processes is the most difficult to quantify, because the problem of transport in fusion plasmas is still unsolved [10]. In the experimental practice it is quantified through a parameter, called energy confinement time, τ_E

[25]. This is defined through the relation

$$W = \frac{P_L}{\tau_E} \tag{11}$$

where $W = wV$ is the total plasma thermal energy, and $P_L = p_L V$ is the total power lost by transport (V is the plasma volume). If, ideally, one could switch of all the heating sources and radiation losses, the energy content would decay exponentially with a time constant equal to τ_E. In stationary conditions, if fusion reactions are absent or negligible, the plasma should be heated with a power P_H equal to $P_L + P_R$. Therefore, since P_H is known, the energy confinement time can be experimentally evaluated. In practice the energy confining time is calculated using scaling laws [26], namely empirical laws deduced from experimental data linking the energy confinement time to the plasma parameters.

We are now ready to state two energy balance conditions. Considering transport contribution, one can define a condition, called ignition [10], in which α-particle heating balances energy losses, and the plasma is self-sustained without external heating ($P_H = 0$). This condition is given by

$$p_\alpha \geq p_b + p_L \tag{12}$$

using the above expressions we end up with the double product

$$n\tau_E \geq \frac{12T}{\langle \sigma v \rangle E_\alpha - 4\alpha_b T^{1/2}} \tag{13}$$

If we now neglect radiation losses and use the approximated expression for the reactivity in absence of temperature profiles the ignition condition reduces to the triple product

$$nT\tau_E \geq 3 \times 10^{21} m^{-3} keV s \tag{14}$$

If we consider density and temperature profiles an even higher threshold is required. In practice, a fusion reactor does not need to reach ignition. Indeed, while this regime might seem advantageous because external heating systems need to be used only transiently to bring the plasma to the required state, shutting them down means that the reactor operator would be lacking a tool to actively control the plasma temperature [10].

Another important parameter is the so-called Q value, which quantifies the ability of the plasma to be a net energy producer. Q is expressed through this formula:

$$Q = \frac{\frac{1}{4} n^2 \langle \sigma v \rangle E_f V}{P_H} \tag{15}$$

so it is the ratio between the produced fusion power and the power required to heat it, Q=1 correspond to breakeven condition, while when $Q = \infty$, ignition is achieved.

The current Q-value record is detained by the JET-Tokamak in UK with a value of 0.67 [27] which is close to the break even condition. ITER, on the other hand, will be the first experiment to cross the Q=1 barrier and produce more energy with respect to that spent [15][16]. Considering also efficiency losses in the trasmutation of thermal energy into electrical energy higher Q values are advisable. For DEMO, the first fusion reactor to be connected to the power grid the foreseen Q-value will be approximately 50 [28].

1.3 Tokamak

Plasma confinement in magnetic fusion devices exploits the fact that charged particles in a magnetic field orbit around the magnetic field lines, and are thus confined, on a characteristic

space scale equals to the radius of the orbit, named Larmor radius ($r_L = \frac{mvc}{qB}$), in the plane perpendicular to the field.

However, particles have a free longitudinal motion, which causes strong losses at the end of the plasma column. The way to overpass this problem consists in closing the magnetic field lines on themselves, i.e. creating a doughnut-shaped configuration, or *torus*.

The simplest way to achieve such a magnetic field is to use coils placed so as to form a toroidal solenoid. This configuration displays poor confinament properties. Indeed, the non-homogenity of the toroidal magnetic field and the curvature of the magnetic field lines introduce a vertical drift, with respect the midplane of the device, inducing a charge separation of ions and electrons and thus creating an electric field. The electric field, itself, coupled with the magnetic field introduces an additional drift pushing both ions and electrons towards the outer part of the plasma torus. This drift motion, which affects both the species, is responsible of poor confinement [10] [7].

The problem of particle drifts can be solved by superposing to the *toroidal* magnetic field component, generated by the coils, a *poloidal* component, which can be generated by a current flowing in the plasma itself, or by further external coils. The superposition of the two components gives rise to helical field lines around the torus. It is common to says that the field has a *rotational transform*. The motion of the particle orbit centers will be also helical, so that the particles will alternatively find themselves in the torus upper part, where the vertical drift will move them away from the equatorial plane, and in the lower part, where the drift will move them towards the equatorial plane. On a full poloidal turn the effects of the drift motion will be eliminated due to these opposite contributions.

The rotational transform can be obtained in the toroidal magnetic configuration named tokamak, Russian acronym, which stands for **to**idalnaya **ka**mera and **ma**gnitnaya **k**atushka, that is "toroidal chamber" and "magnetic coil". It is worth mentioning that other magnetic configurations have been realized in controlled fusion research, such as the Stellarator [29] and the reversed field pinch (RFP)[30].

In tokamaks, the toroidal field component is superposed to the poloidal component, generated by an electric current flowing toroidally into the plasma. The poloidal field is typically smaller than the toroidal one, by an order of magnitude [10].

The toroidal current, also referred as plasma current, is induced by a system of coils, called primary coil in Fig.(6), which is fed with a time varying current. This current causes a variation of the magnetic flux in the torus central hole, which in return, according to Faraday's law, induces a toroidal electric field over the plasma. The toroidal electric field drives the plasma

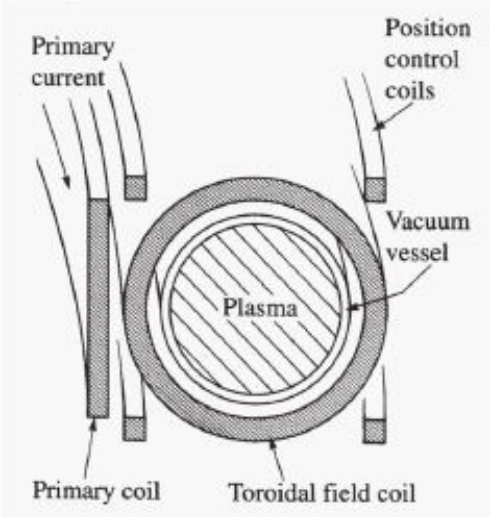

Figure 6: Pictorial representation of a tokamak [10].

current. In practice the plasma acts a the secondary winding of a transformer. The primary winding, also referred as *central solenoid* or *magnetic winding*, are the coils were the time-dependent current is flowing.

Being the plasma current induced, it cannot be sustained steady state forever. The plasma current runs for a period of time, called discharge, and can last from seconds, as in MAST-U, the device investigated in this Thesis, to minutes as foreseen in ITER, the next step fusion prototype which will be described in subsection 1.4. There are methods such as the injection of neutral beams (NBI)[17][18] or electromagnetic waves (Lower Hybrid Resonance Heating [31][32][33]) able to sustain the current and increase the discharge period.

Fig.(6) shows a pictorial representation of the scheme previously described. Note that in the figure there is also a third system composed of coils with current flowing parallel to the plasma current. This system has the role of determining the position and shape of the plasma column. For this reason, these coils are called position control coils.

Conceptual scheme of a reactor As described in the beginning of this chapter, to optimize the power balance, D and T need to be used in fusion reactors. D is a virtually inexhaustible fuel. Being an Hydrogen stable isotope, deuterium can be extracted from water where is present with a concentration of 1 part over 6700 of hydrogen atoms [34]. Tritium is instead unstable and β^--decay to ^{3}He with a half life of 12.3 years. This means that is scarcely present in nature and must be produced in the fusion reactors. The best way to produce it in a reactor consists in exploiting the neutrons, produced by D-T 3 fusion reactions, to fertilize Lithium (Li) [10], according to the following reactions:

$$^6\mathrm{Li} + n \rightarrow \mathrm{T} + {}^4\mathrm{He} + 4.8MeV \tag{16}$$

$$^7\mathrm{Li} + n \rightarrow \mathrm{T} + {}^4\mathrm{He} - 2.5MeV \tag{17}$$

^{7}Li is the main isotope, and the abundance of ^{6}Li and ^{7}Li are 7.4% and 92.6%, respectively. Lithium is a metal which is typically extracted from soil. It is also found in seawater where the element exists at a relatively constant concentration of 190 μg/l [35]. The total lithium content in seawater is very large. It is estimated as 230 billion tonnes and should lead to a widespread and prolonger use of this technology.

The general scheme for the trasmutation of lithium into tritium consists in positioning around the plasma a blanket containing Li. In the blanket, 14 MeV fast neutrons are first slow down by reaction 17 and are finally absorbed through ^{6}Li reaction. The heat released in this process is absorbed by a cooling fluid and converted in electrical power, as sketched in Fig.(7).

It is worth mentioning that the blanket, besides allowing the trasmutation of Li into T and converting the kinetic energy of the 14 MeV neutrons coming out of the plasma into thermal energy, it also screens the coils and other components which would otherwise be invested by a high intensity neutron flux.

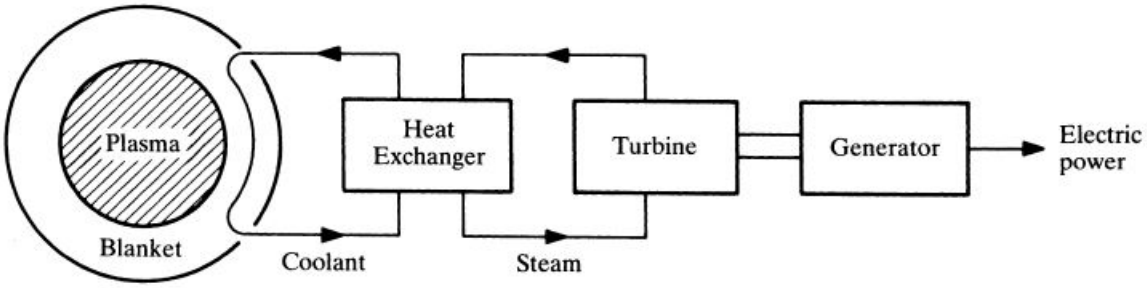

Figure 7: Electric power production in a fusion reactor[10].

1.4 Fusion research trend: ITER

The large experimental database obtained in the last 30 years in several magnetic confinement experiments and the increasing capability of numerical simulations have provided the international community the physics basis for the design of a burning plasma experiment based on the tokamak concept, which is called International Thermonuclear Experimental Reactor (ITER) [15][16].

ITER, located in Cadarache, in the southern France, steams from the collaboration of European Union, USA, China, India, Japan, Russia and South Korea. The project officially started in 1988 and the first plasma is foreseen for 2025 while the first D-T operation will start in 2035. The device is designed for a 20-year lifetime, and it will be the first device ever routinely operating with DT, with all related problems, from radio-protection and material activation [36] to neutron-induced material damage [37]. The main ITER characteristic are summarized in Table(1), while ITER's front view is reported in Fig.(8).

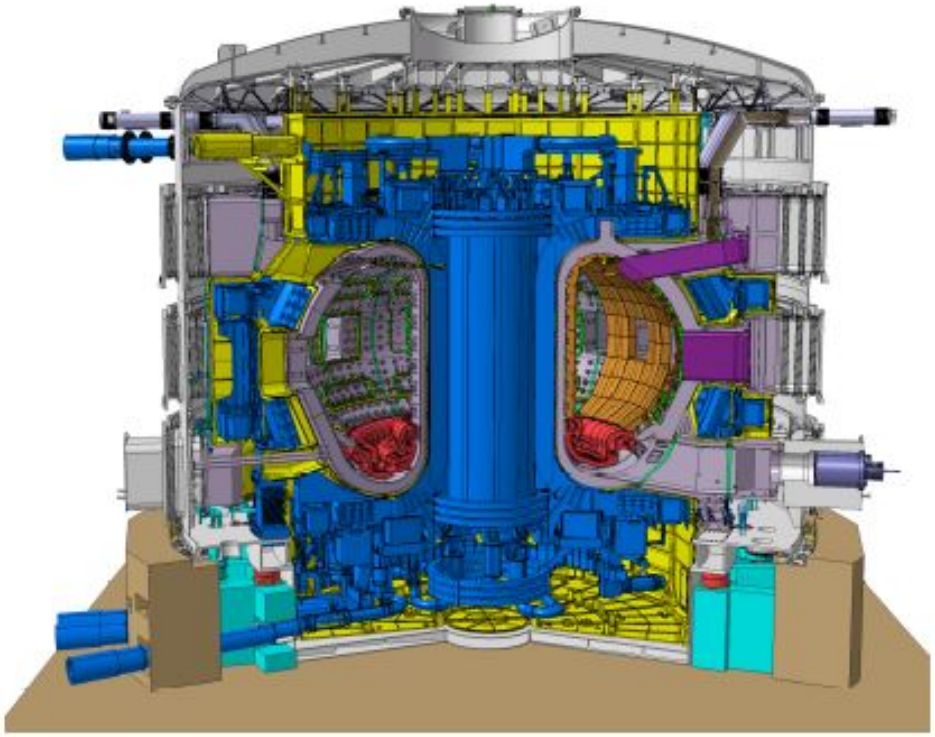

Figure 8: ITER's frontal view. Notice the man at the bottom right to have a comparison [15][16].

Parameter	Design Value
Major radius (m)	6.2
Minor radius (m)	2
Plasma current (MA)	15
On axis magnetic field (T)	5.3
Discharge duration (s)	$\geq$ 400
Energy confinement time (s)	3.7
Heating power (MW)	40
Fusion power (MW)	500
Q	10

Table 1: ITER operational parameters [10].

The main physics goals of ITER are:

- Produce momentarily a plasma of Q=10 i.e. able to generate a 10 times greater fusion energy with respect to the one injected to make it works;
- Maintain an 8 minutes long discharge;
- Operate in a Q=5 steady state;
- Develop technologies and promote research on fusion science and engineering for the creation of a fusion reactor device;
- Demonstrate the safety of a fusion reactor;
- Verify tritium breeding.

To achieve these objectives, a careful optimization of ITER plasma scenarios is needed, which includes the minimization of magnetic field perturbations associated with magneto-hydrodynamics instabilities and spurious magnetic field perturbation. This topics are described in the next sections.

1.5 MHD and instabilities

A plasma can be described differently according to the time and space scales [7]. One can consider it at a microscopic level, and therefore use quantum mechanics, or regard a plasma as the mixture of two fluids, the electron one and the ion one, and apply fluids equations with the suitable modification due to fact that we are dealing with charge particles. Each of these models holds under the appropriate hypothesis. In the following, we introduce two fundamentals parameters when dealing with a plasma: the Debye length and the plasma frequency.

The Debye length is defined as follows:

$$\lambda_D = \sqrt{\frac{k_b T}{8\pi n e^2}} \tag{18}$$

where T is the plasma temperature and n is the plasma density. This quantity represents the typical distance of screening for a charged particle into a plasma. If we are interested in distances longer than the Debye length we can neglect charge separation and therefore consider the plasma as a single fluid. This parameter is also important for what is called the plasma limit i.e. the condition under which a plasma can exhibit collective phenomena arising out of mutual interactions of many charged particles. A collection of charge particles is roughly considered to be a plasma when $g = \frac{1}{n\lambda_D^3} \gtrsim 1$ holds.

The other quantity of interested is the plasma frequency, defined as

$$\omega_p = \sqrt{\frac{4\pi n e^2}{m_e}} \tag{19}$$

This is the frequency at which longitudinal electron charge displacement oscillates inside a plasma. If we deal with times larger than the inverse of the plasma frequency, the plasma can be considered as a single fluid.

The MHD model [10] [7] is a full dynamical theory and holds under the condition of no charge separation and non-relativistic approximation i.e. no terms of order v^2/c^2 or higher are present.

The MHD model includes the following equations:

$$\frac{\partial \rho}{\partial t} + \nabla \cdot (\rho \mathbf{v}) = 0 \tag{20}$$

$$\frac{\partial \mathbf{v}}{\partial t} + (\mathbf{v}\cdot\nabla)\mathbf{v} = \mathbf{F} - \frac{1}{\rho}\nabla\left(p + \frac{B^2}{8\pi}\right) + \frac{(\mathbf{B}\cdot\nabla)\mathbf{B}}{4\pi\rho} + \nu\nabla^2\mathbf{v} \tag{21}$$

$$\frac{\partial \mathbf{B}}{\partial t} = \nabla\times(\mathbf{v}\times\mathbf{B}) + \frac{c^2}{4\pi\sigma}\nabla^2\mathbf{B} \tag{22}$$

Eq.(20) is the usual continuity equations typical of fluids. Eq.(21) is the Navier-Stokes equation with the addition of Lorentz force suitably rewritten in terms of the only magnetic field with ν the viscosity. In particular the term $B^2/8\pi$ is the magnetic pressure and $(\mathbf{B}\cdot\nabla)\mathbf{B}$ represent the magnetic tension i.e. the tension along magnetic field lines. Eq.(22) is the induction equation which is a novelty of MHD and describes the change in time of the magnetic field, where σ is the conductivity. The second term of the right hand side of induction equation shows a diffusive character of the magnetic field. In the case where resistivity can be neglected the induction equation allows to formulate the Alfvén's frozen flux theorem [7], which states that magnetic field lines behave like if it were frozen into the plasma. This effect has strong consequences in magnetic topology and in stability of a plasma.

An important quantity which is associated with MHD stability is the safety factor. This name steams from the role that this quantity plays in the stability of confined plasma and it is defined as

$$q = \frac{\Delta\phi}{2\pi} \tag{23}$$

where $\Delta\phi$ is the magnetic field line angular distance travelled toroidally for a full poloidal turn. It is a measure of how loosely are the magnetic field line winded around the torus. Thus, if a field line comes back to its poloidal starting position after making exactly one toroidal turn around the torus, it will have q = 1. High q values correspond to a loosely wound helix, and viceversa. The q values corresponding to rational numbers play an important role in plasma stability. Indeed, they identify the locations of where MHD instabilities can be located.

A possible classification of the instabilities is the distinction between i) ideal modes, which are the instabilities described within the framework of ideal MHD, that is a version of MHD where the resistivity is neglected, ii) resistive modes, which depend on the finite plasma resistivity.

In general, it is possible to say that if a plasma is ideally unstable, it will be unstable also if finite resistivity is taken into account. Indeed, ideal modes are the most violent instabilities which can take place in a magnetized plasma, have very fast growth rates, and lead almost invariably to premature discharge termination. Resistive modes do not necessarily bring to discharge termination, but have negative effects on plasma confinement, since they can modify the magnetic surface topology.

In some situations, resistive modes can destroy the magnetic surfaces, giving rise to field lines which fill ergodically a region of space: in this region the confinement will be poor. Both ideal and resistive instabilities have an infinite spectrum of normal modes.

In the simple case of a circular plasma with large aspect ratio, these modes depend on the poloidal and toroidal angles as $exp[i(m\theta + n\phi)]$, where m and n are integer numbers called poloidal and toroidal wavenumber. The perturbation mode has therefore an helical wavefront. Since fusion plasmas are very hot the magnetic field lines are frozen inside the plasma for the Alfvén's frozen flux theorem. Therefore, the magnetic field lines will oppose any attempts to increase their curvature or to compress them against each other. We can understand that the more violent modes are those for which the resonant condition $q = -\frac{m}{n}$ holds. In this case, the pitch of the perturbation wavefront is the same of the magnetic field lines meaning that the perturbation causes a displacement which does not compress or bend the magnetic field lines.

Figure 9: Bending of the plasma column [7].

In order to have resonant condition q must be a rational number therefore this condition holds on the so called *rational magnetic surfaces*.

Over the years of magnetic fusion research, several MHD instabilities have been identified, such as the kink and the tearing mode, which are briefly described on the following.

One of the strongest ideal MHD instability is the kink instability [38] which causes the bending of the plasma column. A slight bending of the plasma column indeed grows as an instability, due to the magnetic pressure, which will be higher in right side of the plasma, as shown in Fig.(9).

Kink modes have fast growth rate quantifiable as the inverse of the Alfvén time, namely

$$\tau_A^{-1} = \frac{B}{a\sqrt{4\pi\rho}} \tag{24}$$

This instability can be slowed down by placing a conductive wall around the plasma [39]. During the evolution of the kink mode eddy-currents are induced inside the conductive wall which oppose the plasma motion and have a stabilizing effect. The typical time of the kink instability is therefore increased to the resistive diffusion of the magnetic flux through the wall $\tau_r = 4\pi\sigma a\delta/c^2$ with δ the width of the wall, σ its conductivity and a the tokamak minor radius.

Another possible instability is the tearing mode [40]. As the name suggests, this current driven instability causes the tearing and reconnection of magnetic field lines. It is produced by a strong gradient in the current density profile parallel to the magnetic field lines. The change of magnetic topology associated with this mode implies that a finite resistivity must be take into account in the MHD model. Magnetic reconnection occurs in region called *current sheet* where steep gradient in the current causes the Alfvèn's frozen flux theorem not to hold. During the reconnection of magnetic field lines, magnetic island can be formed i.e. regions with a different magnetic topology.

It is worth anticipating that during the execution of the compass scan technique, a method used to identify spurious magnetic field errors, such kind of instability has been triggered and investigated in this Thesis work.

1.6 Error fields

In magnetic fusion devices, spurious non-axisymmetric magnetic field perturbations, typically called error fields, can be present and are due to:

- misalignment introduced in the construction of the device;
- imperfections in the manufacture of the field coils;
- 3D structures in the wall surrounding the plasma;

- current feeds;
- presence of ferromagnetic materials near the plasma surface [1].

The presence of error fields can have a large impact on energy confinement and plasma stability. For example, components of error fields can resonate at low order rational surfaces, usually the n=1, and can induce a magnetic island at the q=2 surface, the most detrimental plasma instability. At low levels of error field amplitude, magnetic reconnection is suppressed by the plasma rotation. As the error field is increased in amplitude, above a critical value a sharp transition occurs, where the plasma rotation is quickly brought to zero and a non-rotating, or locked magnetic island is seen to grow. This effect is known as magnetic field penetration [3], and leads to the termination of the plasma discharge, or plasma disruption.

Error fields can also have detrimental effects on plasma performance by damping plasma rotation through the neoclassical toroidal viscosity torque, by inducing fast particle losses and by triggering ideal-MHD instabilities when exploring high-beta regimes. Moreover error fields represent a limiting aspect for some operational regimes such as low density plasmas.

Because of this brute effects, error fields in fusion devices need in primis to be detected and robust strategies to correct them, i.e. reduce their amplitude, have to be applied.

1.6.1 Error fields identification

To detect error field, an experimental technique, named compass scan [41], is usually executed. This technique, which has been utilized in various fusion devices, such as AUG, ALCATOR C-MOD, DIII-D, JET, MAST, NSTX-U, T2R and RFX-mod, consists in applying a probing magnetic field of known phase and amplitude to a reproducible low-density Ohmic plasma. This probing magnetic field is induced by current in the correction coils, which are breafly described in subsubsection 1.6.2.

When executing the compass scan, as the magnetic field is composed of a linear superposition of magnetic fields, the plasma will respond to both the applied perturbing field and the intrinsic error field. By varying the amplitude and the phase of the probing field, the response of the plasma to the external perturbation is investigated. In particular, when the toroidal phase of the probing field coincides with the toroidal phase of the intrinsic error field, a sudden increase of the normal magnetic field component occurs at lower probing field amplitude. Conversely, when the toroidal phase is opposite to the toroidal phase of the intrinsic error field, a sudden

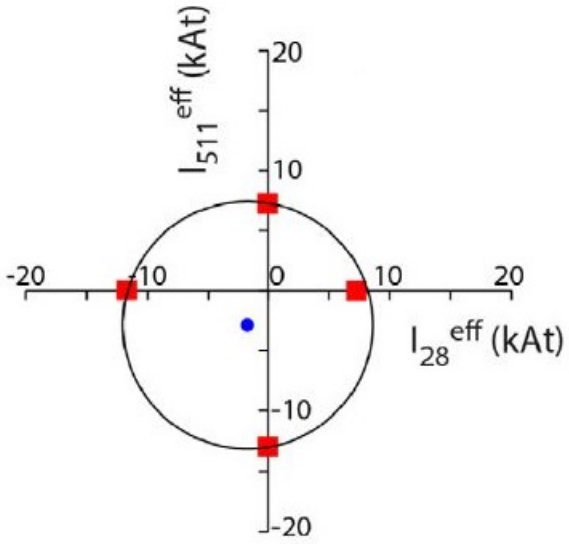

Figure 10: Results of compass scan in MAST device [42].

increase of the normal magnetic field component occurs at higher probing field amplitude. The increase of the normal magnetic field component is due to the triggering of a locked mode, a non-rotating m=2, n=1 magnetic island, which forms when the field penetration process takes place.

The compass scan allows the identification of the error field correction currents. Indeed, by calculating the current in the correction coils at the locked mode triggering, and reporting this data in a polar plot, a circle can be identified. Without error field sources, the circle is centered at the origin. Conversely, if the circle is shifted and error field is present and the centre of the circle yields the optimum error field correction currents.

Fig.(10) shows, as an example, the results of a compass scan, which has been executed in MAST device [42]. Note that in this case, the center of the circle is not centered at the origin, so a non negligible error field needs to be compensated.

1.6.2 Error fields correction

The reduction of error field can be pursued with two methods:

- Passive control which consists in a careful alignment of coil position to compensate the n=1 error field. This is achieved by identifying the optimal coil shift and tilt. This procedure has been applied when assembling MAST-U device [1] and implies the installation of coils considering relatively small tilts and shifts, of the order of some mrads and some mms, respectively.
- Active control which exploits the presence of in and (or) ex-vessel coils to induce a magnetic field pattern designed to minimize the EF amplitude.

Fig.(11) shows, as an exampled, the error field correction coils scheme installed in the DIII-D tokamak, at General Atomics, San Diego, California, and in ITER [43]. DIII-D is equipped with 2 set of error field correction coils: the C, an external band of six coils, located at the midplane and the I coils, two internal bands of six coils. On the other hand, ITER will have three external bands of six coils for error field correction, located at the midplane, top and bottom of the vacuum vessel.

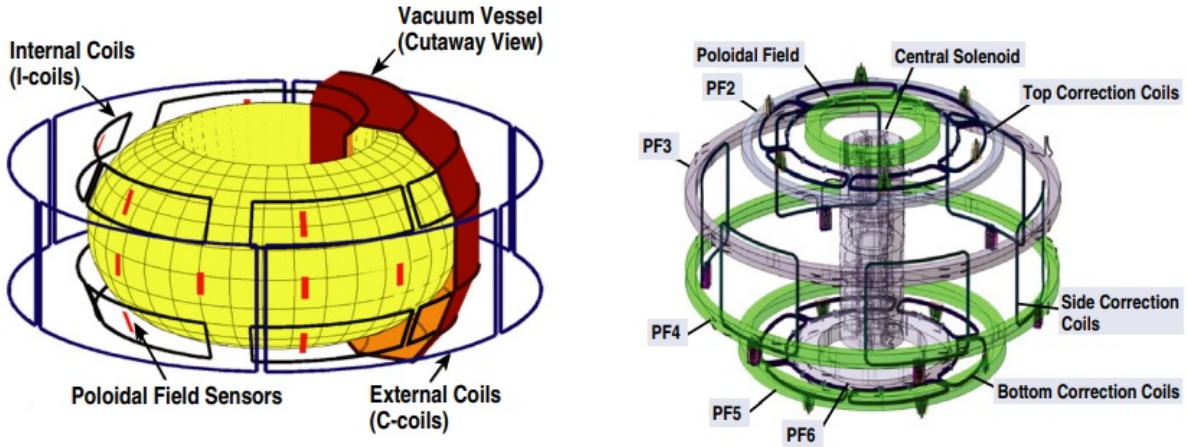

(a) (b)

Figure 11: Scheme of DIII-D (a) and ITER (b) correction coils [43]. (a) An external band of six coils (C-coils) at the midplane, and two internal bands of six coils each (I-coils) for DIII-D. (b) Three external bands of six coils for error field correction, located at the midplane, top and bottom of the vacuum vessel for ITER.

1.7 Objectives of this Thesis project

MAST-U (Mega Ampere Spherical Tokamak Upgrade), located at the Culham Centre for Fusion Energy, Oxfordshire, England, is the upgrade of MAST machine, which ran from 2000 to 2013. A sketch of MAST-U device is shown in Fig.(12)

The research program of MAST Upgrade is oriented towards compact fusion power plants, testing reactor technology and addressing physics issues for the international ITER fusion project, as described in subsection 1.4. It has been rebuilt to enable improved performance, namely longer pulses, increased heating power and a stronger magnetic field and to contribute on plasma exhaust studies, thanks to the installation of a modular divertor, which can be configured as Super-X, snowflake and long-inner leg.

The main new features of MAST-U are 6 poloidal coils and 14 divertor coils, which allow the realization of the divertor configurations aforementioned. On the other hand, the poloidal field coils named P4 and P5, which have been identified as the main source of error fields during MAST operations, have been retained in the upgrade [3] [42].

To minimize the impact of error fields on plasma performance and on the available opera-

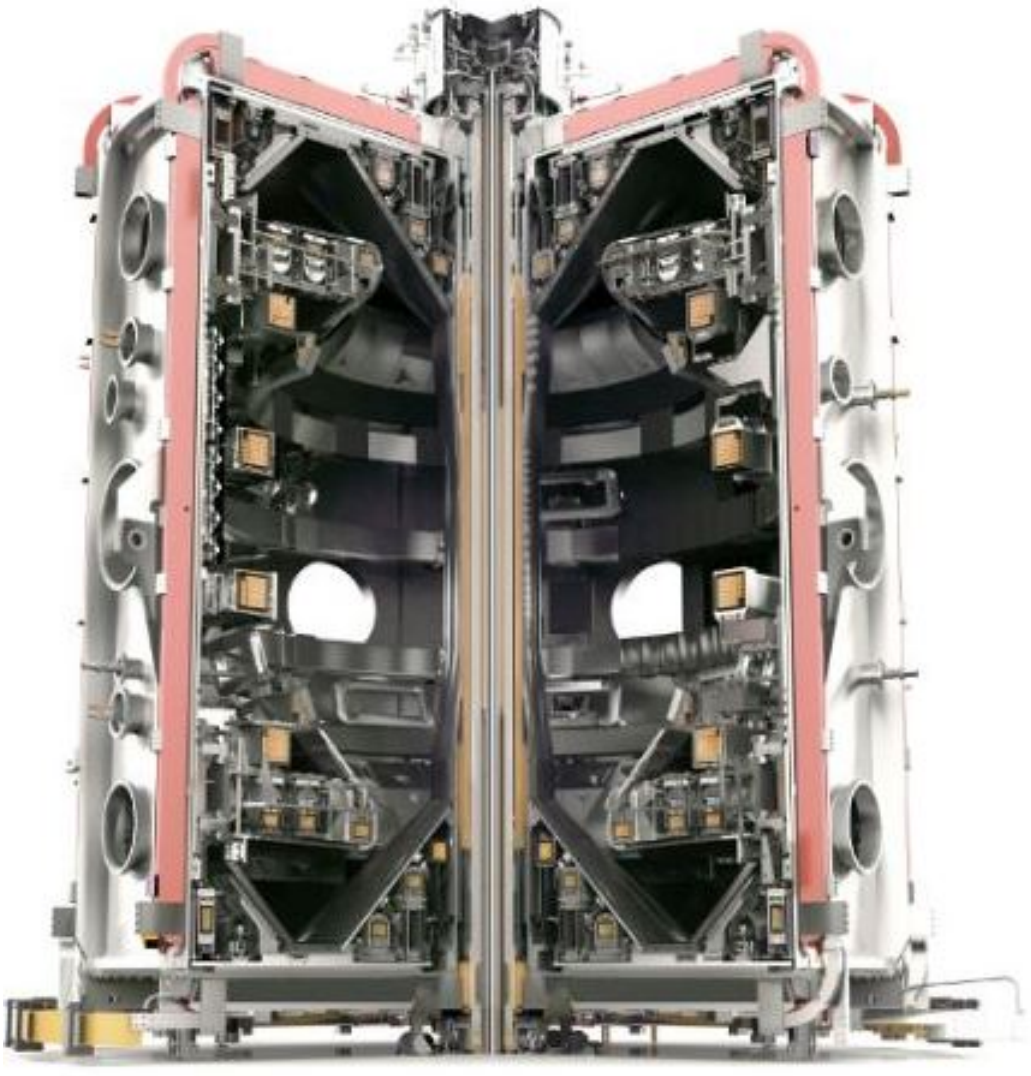

Figure 12: MAST-U cross section showing the internal coils.

tional space in the new MAST-U device, it is important to identify the error field sources and develop error field control strategies for their minimization.

As anticipated in the previous section, to minimize the n=1 error field component, a passive error field control strategy has been adopted when assembling MAST-U. This strategy consists in applying relatively small tilt and shift when installing the poloidal and the divertor coils, which guarantees n=1 error field minimization. The optimal coil alignment has been determined based on magnetic field measurements and the corresponding 3D electro-magnetic modelling[1].

To assess the presence of residual n=1 error field sources in MAST-U, dedicated experiments have been performed in the framework of FP9 Horizon program WorkPackage Tokamak Exploitation RT01: ITER baseline scenario towards detachment and low collisionality. These experiments have been analyzed within this Thesis project with the following objectives:

- Identify the n=1 error field.
- Assess possible scaling law of locked mode with the main plasma parameters, i.e. density.

In the following chapters, after a brief introduction on MAST-U device and the diagnostic involved in this work, a method based on the transfer function identification is presented. Such a technique allows the calculation of the external field, and thus the plasma response, which is the key metrics to investigate the locked mode onset and deduce the empirical error field correction currents.

2 The MAST-U device and the main diagnostics

In this chapter, MAST-U device and its capabilities are described, together with the main diagnostics involved in this work: saddle coils, the interferometer and the D_α detector.

2.1 MAST-U Device

This Thesis work has been focused on analyzing data from the MAST-U (Mega Ampere Spherical Tokamak Upgrade) device, which is a spherical tokamak located at the Culham Centre for Fusion Energy, Oxfordshire, England.

Spherical tokamaks are characterized by an aspect ratio, namely the ratio between the torus major radius and minor radius, smaller than the one in a conventional tokamak. Fig.(13) is a sketch which shows the different layout between a convectional (on the left) and a spherical (on the right) tokamak.

The main advantage of operating a spherical tokamak is the possibility to reach values of β, defined as $\beta = \frac{\overline{p}}{B^2/8\pi}$ (where the numerator is the plasma pressure and the denominator is the magnetic pressure), higher with respect to conventional tokamaks, typically of one order of magnitude. This allows, with the same magnetic pressure, to reach higher temperatures, meaning better power balance [10] [7].

MAST-U device is based on the original MAST machine, which ran from 2000 to 2013. The main design machine characteristics are summarized in Table(2), while the device operational parameters are reported in Table(3).

MAST-U has been designed to enable higher performance, namely longer pulses and increased heating power, to achieve a stronger magnetic field and especially to contribute on

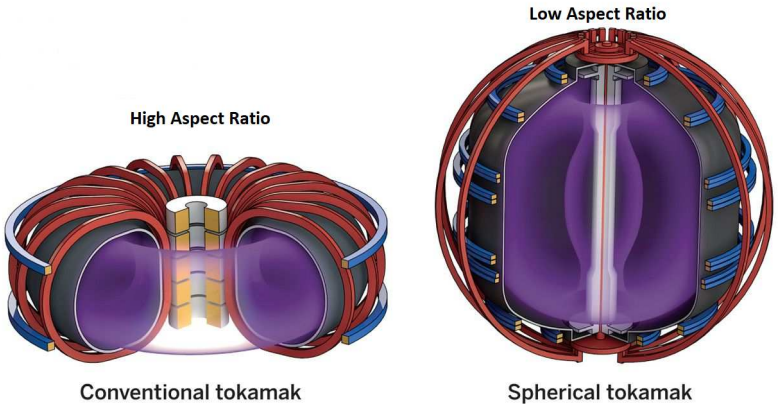

Figure 13: Aspect ratio comparison. Left: Conventional tokamak with high aspect ratio. Right: Spherical tokamak with low aspect ratio.

Parameter	Design Value
Major and minor radii (m)	0.7/0.5
First wall material	Carbon graphite
Maximum toroidal magnetic field (T)	0.8
Maximum plasma current (MA)	2.0
Plasma heating	up to 6 MW
Ohmic heating	0.2 - 1 MW
Neutral beam injection heating	5 MW for 2s, deuterium beam
Injection energy	75 keV, 50-75 keV possible

Table 2: Design parameters of MAST-U.

Parameter	Design Value
Pulse duration	Typical 2 s, maximum 5 s
Time between pulses	15 min for 2 s pulses, 30 min for a full duration pulse
Main species	H, D, He
Electron density	$1.5\times10^{20}m^{-3}$
Electron temperature	up to 3 keV
Ion temperature	up to 3 keV
Normalised β_N	4-6

Table 3: Operational parameters of MAST-U.

plasma exhaust studies, a key issue that must be solved to achieve commercial fusion energy. Indeed, because of a not perfect confinement, particles can leave the plasma and through a set of coils, named divertor coils, their energy can be deposited in dedicated region, called the divertor plates.

To withstand high power loads, in MAST-U 14 up and down symmetric divertor (D) coils have been installed, named D1, D2, D3, DP, D5, D6 and D7, shown in Fig.(14). This new coil set allows to test the 'Super-X divertor' configuration. This is a sophisticated exhaust system, designed to reduce heat and power loads on the divertor region, which should translate in long lasting divertor components. It is also worth mentioning that in MAST-U, besides Super-X divertor, other divertor configurations can be realized, such as snowflake and long-inner leg.

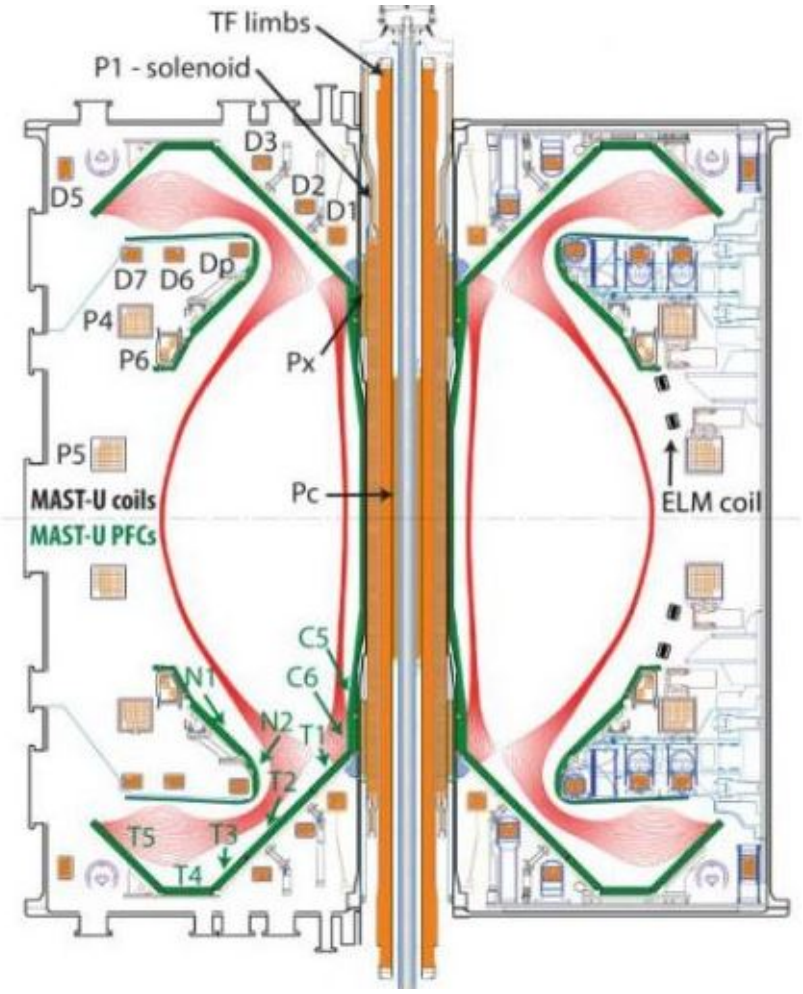

Figure 14: MAST-U coils: divertor, poloidal, ELM coils and plasma facing components.

MAST-U offers the possibility to explored a wide range of operation scenarios: Ohmic L-Mode, NBI assisted L-Mode and NBI assisted H-Mode.

In particular, the database analyzed in this work consists of 90 shots in Ohmic L-mode realized in the framework of FP9 Horizon program, WorkPackage Tokamak Exploitation RT01: ITER baseline scenario towards detachment and low collisionality. In this experiment, the presence of error field correction coils (EFCCs) has been exploited to identify the intrinsic n=1 error field source in MAST-U, as described in section 1.

The EFCCs, retained from MAST, consist of four coils arranged symmetrically around the outside of the MAST-U vacuum vessel and are located at R = 2.9 m. Each coil is about 4 m high, i.e. -2 m $\leq$ Z $\leq$ 2 m, being made up of 3 turns and can carry up to 5 kA/turn. This coil set has been arranged in n=1 configuration, and each coil pair is named EFCCs NESW and EFCCs NWSE.

2.2 Saddle coils

MAST-U is equipped with a wide coverage of magnetic field sensors, which can detect the normal, or radial, and the tangential, or poloidal, magnetic field components. The information collected by magnetic field sensors, as saddle coils, Mirnow coils, Rogowskis, Halo current detectors and diamagnetic loops, allows for equilibrium reconstruction, analysis of MHD activity, plasma control and machine protection.

In this Thesis work, magnetic sensors, which measure the radial magnetic field component, i.e. saddle coils, have been analyzed. Signals from saddle coils indeed contain a clear signature of the locked mode onset, which is the dynamics we are interested in. The name saddle coil is a hang over from the old days where a coil attached to the outside of the vacuum vessel would have formed a saddle shape.

A saddle coil is a loop of wire placed near the plasma at a suitable angle. Changes in the magnetic field flux through the loop induce an electric current on the loop itself by Faraday's law. The current is sustained by a voltage which can be easily measured. The knowledge of the voltage, together with the geometric properties of the loop, allows to determine the value of the magnetic field.

MAST-U is equipped with 3 sets of saddle coils: 12 wall saddle coils, 2 $\times$ 6 center column saddle coils and 2 $\times$ 24 top-bottom saddle coils, as shown in Fig.(15). Among these saddle coil sets, the signals from the 12 wall saddle coils have been analyzed to calculate the n=1 radial magnetic field components, as described in section 3.

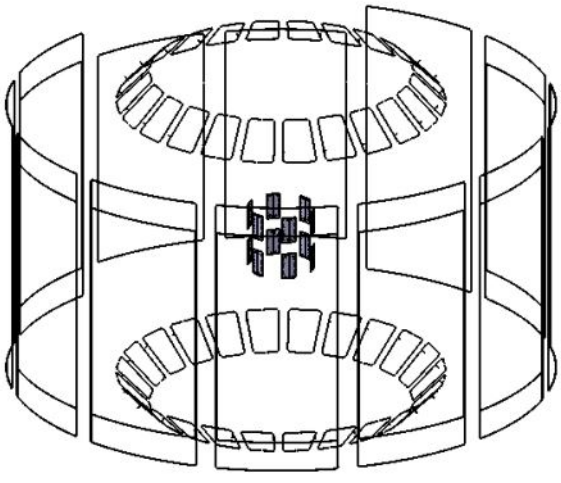

Figure 15: Location of the saddle coils in MAST-U device.

2.3 Interferometer

Plasma density is one of the fundamental plasma parameters in a fusion device. It directly determines the plasma performance and thus is continuously monitored and controlled. This is particularly important also for scenario development, from the point of view of operation limits, such as the Greenwald limit [44] or the low density limit, which can be responsible of electron runaway population [10].

In fusion devices, the most common diagnostic used to measure the plasma density is the interferometer, which is equipped with line of sights (LOS). The measure is based on the variation in optical path length between two measurement arms which pass through mediums with different refractive index.

Fig.(16) shows a sketch of the Michelson-Morley interferometric setup used in MAST-U interferometer. A coherent light beam, usually sourced by a laser, is split into two different beams using a beam-splitter. One beam arm, usually referred to as the scene arm, passes through a dispersive medium with its refractive index (plasma in this case), the another, usually referred to as the reference beam, passes through a second arm without a perturbed refractive index (typically air). The optical path length between the two arms differs both according to their spatial length difference and the difference in refractive index. The beams are recombined at a detector and the phase difference between the two is measured against some previously defined null-value using the interference pattern. If the interferometer is equipped with two arms of the same length, the path difference can be traced back to the line integral of the density of the medium.

Usually, the density is expressed as an volume averaged quantity. To perform this calculation, the line averaged density is normalized to the length of the LOS. The length of LOS can be easily calculated, once known the plasma shape.

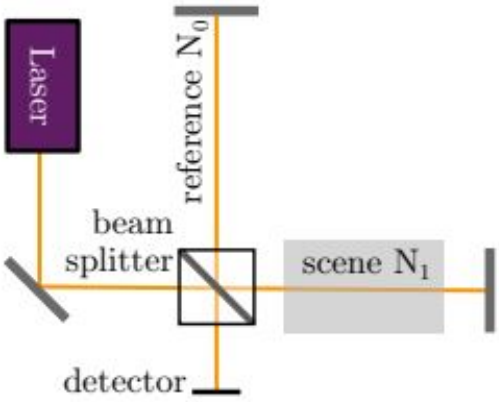

Figure 16: Basic schematic of a Michelson-Morley interferometer. The optical path length between the two arms differs according to the difference in propagation speed.

2.4 D_α detector

D_α detector measures the red light emitted by excited deuterium atoms. In MAST-U, optical fibre and collimator lens are used to collect the emitted photons. This light is then delivered to the filterscope i.e. a lens able to collimate the light out of the fibre. After that the D_α filter isolates the electromagnetic radiation emitted from deuterium atoms, which is finally injected in the Photo-multipliers (PMTs).

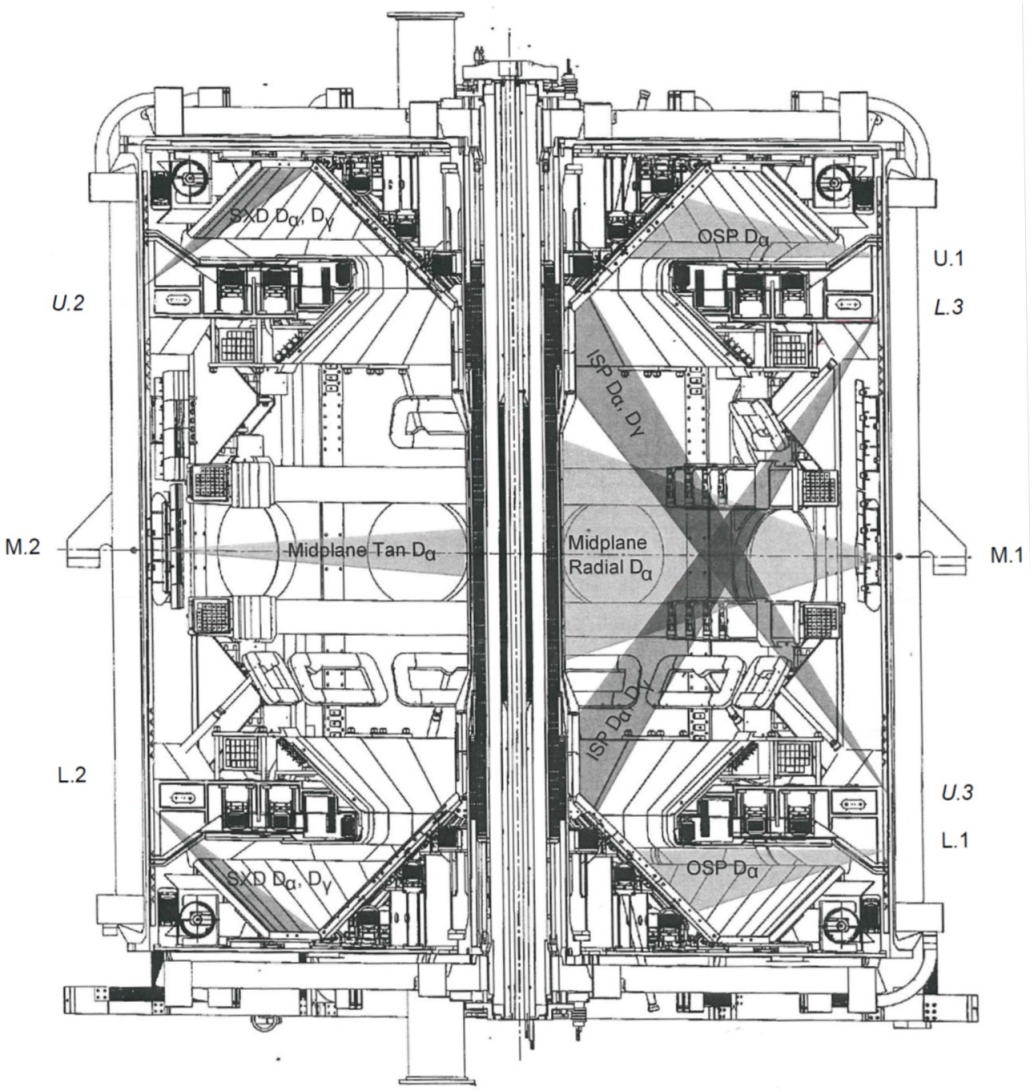

Figure 17: Fields of view of D_α detectors.

MAST-U is equipped with many fields of view on the plasma, as shown in Fig.(17). Each label reported in the figure identifies a specific view. The analysis carried out in this work uses the D_α signal coming from the tangential mid-plane view covering a radius of approximately 1.4 m and a narrow field of view of 5°.

3 AC compensation of magnetic signals

In this chapter, the approach adopted to identify the transfer functions between MAST-U actuators, i.e. error field correction, toroidal field, divertor and poloidal coils, and the n=1 radial magnetic field components is presented. Such an analysis has been performed to develop a tool capable of calculating the external magnetic field, a quantity, which needs to be subtracted from the total magnetic field, to calculate the plasma response.

3.1 Transfer function identification

One of the objective of this Thesis work is the detection of locked mode onset in compass scan experiments. As described in subsection 2.2, signals of saddle coils are mostly analyzed for this scope since they can detect the radial magnetic field perturbations due to this mode. However, the saddle coil sensors, not only detect the plasma activity, i.e. B_{plasma}, but also the magnetic field contributions given by the various coils which are energized during the plasma discharge, i.e. pick-up, B_{ext}.

For determining the time of the locked mode onset, it is of paramount importance to identify with some methodology such spurious magnetic field contributions and subtract them from the total magnetic field, namely B_{plasma}+B_{ext}.

The approach adopted to compensate the total radial magnetic field from external magnetic field sources deploys the identification of the transfer function (TF). The transfer function $H(s)$ of a system, sub-system, or component is a mathematical function which theoretically models the system's output for each possible input [45]. It is define as the ratio,

$$H(s) = \frac{\mathcal{L}[O(t)]}{\mathcal{L}[I(t)]} \tag{25}$$

where $\mathcal{L}[O(t)]$ and $\mathcal{L}[I(t)]$ are the Laplace transforms [45] of the output and input signals while s is the complex frequency i.e. $s = \sigma + j\omega$ with σ, $\omega \in \mathbb{R}$. The real part σ is related to the amplitude of the signal while the imaginary part is the usual frequency. In practice the complex frequency is a generalization, of the usual frequency, which takes into account also the damping or growth of a signal. The transfer function is usually expressed as the ratio of two polynomials:

$$H(s) = G\frac{(s-a_0)(s-a_1)...(s-a_n)}{(s-b_0)(s-b_1)...(s-b_m)} \tag{26}$$

where $a_0...a_n$ and $b_0...b_m$ are the zeros (Z) and the poles (P) of the transfer function, while G is the gain factor. Poles have an important role in terms of stability of a system i.e. finite response for finite input. It is easy to observe that a system cannot be stable if it exist a pole with positive real part.

The magnetic data analyzed in this Thesis work has been acquired by an array of 12 saddle coils, located external to the vacuum vessel, as described in subsection 2.2. Since the n=1 locked mode dynamics needs to be investigated here, the n=1 radial magnetic components have been extracted from saddle coil measurements.

If ϕ_i refers to the saddle coils' toroidal position and y_i is the measured signal, the n=1 sine (S) and cosine (C) components of the radial magnetic field (B_r) can be calculated as follows:

$$\begin{cases} S = \sum_{i=1}^{12} y_i sin(\phi_i + \frac{\pi}{4}) \\ C = \sum_{i=1}^{12} y_i cos(\phi_i + \frac{\pi}{4}) \end{cases} \tag{27}$$

Shot	Coil
44430	TF
43322	P1
43812	P4
43811	P5
43740	P6
43326	PX
43825	D1
43826	D2
43828	D3
43829	DP
43830	D5
43831	D6
43832	D7
45417	EFCCs NESW
45418	EFCCs NWSE

Table 4: 15 Vacuum shots used for TF identification.

In order to perform the identification of the transfer function (TF) between each actuator (P and D coils, EFCCs in n=1 configuration, toroidal field coil) and the n=1 B_r components, a database of 15 ad-hoc vacuum shots was collected. In these vacuum shots, which are discharges without plasma, each coil set has been fed independently with the maximum allowed current level, to improve the signal/noise ratio, and the current has been ramped up as fast as possible to detect the time dependence, or AC couplings, of the TF. Table(4) reports the vacuum shots used for TF identification.

As described before, the n=1 B_r magnetic signals have been expressed in terms of sine e cosine components. This implies that for each coil fed, two transfer functions have to be identified.

The procedure for the TF identification is performed with the System Identification Toolbox [46], available in MATLAB environment based on two built in functions, i.e. *tfest* and *lsim* [47][48]. Function *tfest* estimates a continuous-time transfer function using the time-domain or frequency-domain data starting from a model of given number of zeros (Z) and poles (P) whilst *lsim* plots the simulated time response of the estimated system model to the input experimental data, which is this case is the coil current. The choice of the model to be used was a compromise between simulated-experimental data agreement and the complexity of the model itself. The agreement between the experimental data and model prediction is quantified in term of the *fitpert* parameter, which is expressed as follows:

$$fitpert = 100\left(1 - \frac{y - y_1}{y - mean(y)}\right) \tag{28}$$

where y is the experimental data and y_1 is the simulated one. In other words, *fitpert* indicates how well the predicted response model matches the measurement, which is the n=1 B_r component.

The identification of the TF has been carried out for all the discharges reported in Table(4), and the corresponding results are described in this chapter and reported, for completeness, in appendix (section 6).

The identified TFs have been implemented in a matrix, called $M(\omega)$, which allows the calculation of the external magnetic field, namely B_{ext}, induced when EFCC, P, D and toroidal field coils are fed with some level of current. It is worth stressing that such matrix is a powerful

tool. Indeed, it can be used for signal compensation for every shot, once the currents in EFCC, P, D and toroidal field coils are known.

M(ω) has played a major role when analyzing compass scan experiments. As described in the next chapter, the locked mode onset needs to be identified in this kind of experiment. The identification can be misleading or biased if a non objective procedure would be adopted.

To retrieve the locked mode onset, the plasma response is the metrics that needs to be calculated. It is indeed a key quantity, able to describe the MHD dynamics in the plasma of interest.

The plasma response can be calculated by subtracting from the total radial magnetic field, the external magnetic field. By analyzing the behaviour of the plasma response, the identification of the locked mode onset is straightforward and can be completely automated implementing a suitable algorithm.

In the following subsections, examples of TF identification, for one set of EFCC, a P coil and a D coil are presented.

3.1.1 The TF of EFCCs

MAST-U error field correction system consists of four coils arranged symmetrically around the outside of the vacuum vessel. Routinely, these coils are arranged in pairs, with opposite coils wired in series to produce a n=1 non-axisymmetric magnetic field. These coil pairs are powered by independent power supplies, and are named 'EFCC NESW' and 'EFCC NWSE'.

The vacuum shot 45418, analyzed to identify the TF among EFCC NWSE and the n=1 radial magnetic field components, is presented here as an example. In this discharge, as shown in Fig.(18)(a-b), only EFCCs NWSE has been fed with some level of current. The induced n=1

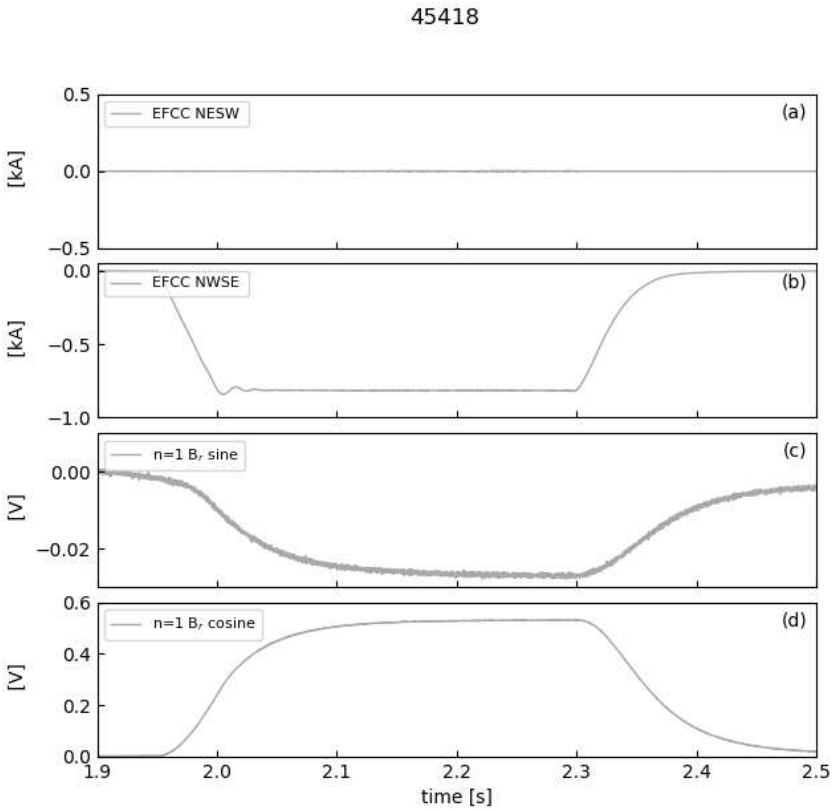

Figure 18: Time behavior of (a) current in NESW EFCCs (b) current in NWSE EFCCs (c) filtered n=1 B_r sine component (d) filtered n=1 B_r cosine component. Data refers to 45418 vacuum discharge.

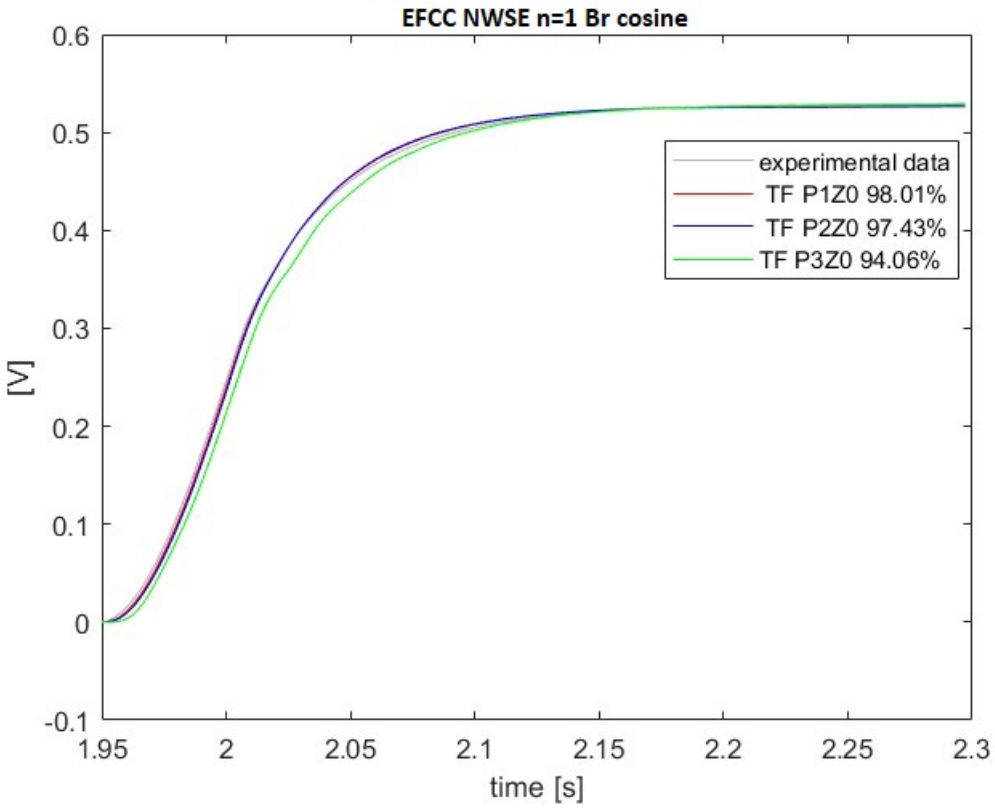

Figure 19: Comparison of the *fitpert* parameter for three models tested for the n=1 B_r cosine component.

radial magnetic field sine and cosine components, derived from saddle coil measurements, are reported in Fig.(18)(c-d), respectively.

These quantities have been filtered using a Simple Moving Average filter (SMA [49]) to reduce the noise, which could be present in the signals, and analyzed in the MATLAB framework to identify the TF.

The MATLAB System Identification Toolbox allows to define various models of TF with given zeros and poles. Fig.(19) represents a series of modelled n=1 B_r cosine components, obtained varying the number of poles and zeros. In particular, the following TFs have been modelled: P1Z0 in red, P2Z0 in blue, P3Z0 in green. Note that among the TF models investigated, the one that results in better agreement with the experimental data is P1Z0, as demonstrated by the highest *fitpert* parameter obtained, which is 98.01%.

Fig.(20)(a,b) show the comparison among the experimental data and P1Z0 modelling results for both the n=1 B_r components. Besides the *fitper* indicator, also the residual, i.e. the difference among the experimental data and the modelling results has been calculated and has been reported in Fig.(20(c,d), for the n=1 B_r sine and cosine components, respectively. Note that the residual amplitude is relatively small, below the 10 mV threshold, which has been considered to be an acceptable discrepancy between simulated and experimental data.

The expressions of the estimated transfer functions are:

$$\begin{cases} H_{sin}(s) = \dfrac{0.59}{s + 18.9} \\ H_{cos}(s) = -\dfrac{17.97}{s + 27.8} \end{cases} \tag{29}$$

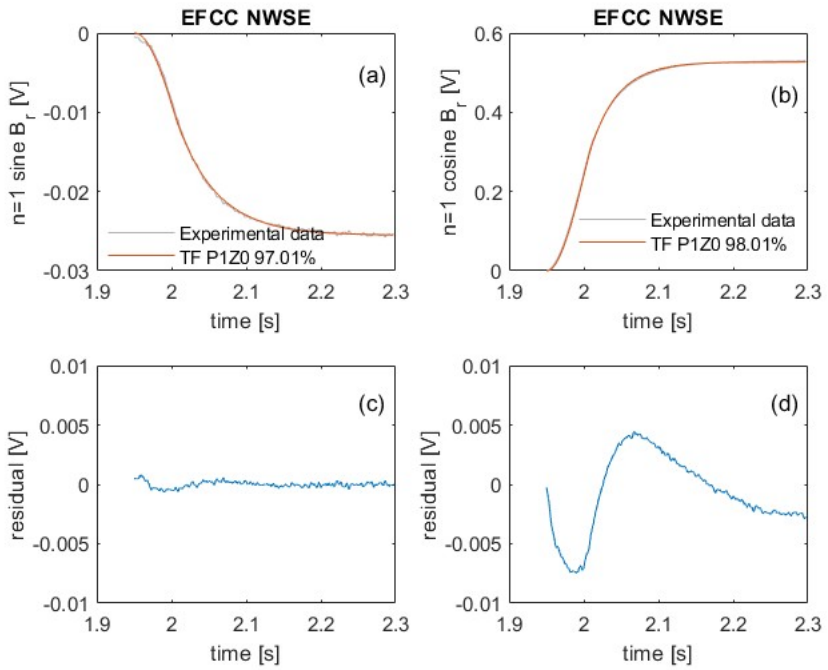

Figure 20: (a) Comparison between the simulated data, using a model with a single pole i.e. P1Z0, and the n=1 B_r sine component. (b) Comparison between the simulated data, using a model with a single pole i.e. P1Z0, and the n=1 B_r cosine component. (c) Residual of n=1 B_r sine w.r.t the simulated data. (d) Residual of n=1 B_r cosine w.r.t the simulated data.

3.1.2 The TF of P1 coil

The MAST-U device is equipped with 9 poloidal field coils. Here, as an example, the identification of the TF between the P1 coil, placed at the center of the device, and the n=1 B_r components is presented. For this scope, 43322 vacuum shot has been analyzed.

Fig(21)(a) shows the current behavior in P1 in this discharge, while in Fig(21)(b,c) the induced n=1 B_r sine and cosine signals are reported. As described in the previous subsection, the data presented in this figure has been processed to identify the TF using MATLAB System Identification Toolbox. Various poles and zeros combinations have been tested to identify among the various TF models the one able to describe the system.

Fig.(22) represents the results of these tests for the n=1 B_r cosine component, where the number of poles and zeros have been varied considering the following TFs: P1Z0 in red, P1Z1 in blue and P2Z0 in green. Note that among the TF model investigated, the one that results in better agreement with the experimental data is P1Z0, as demonstrated by the highest *fitpert* parameter obtained, which is 92.09%.

The same procedure has been applied to identify the TF among P1 and the n=1 B_r sine component. In this case, the model which is able to better describe the couplings between P1 coil and the n=1 B_r cosine component is given by P2Z1 with 95.96% of *fitpert*. The comparison among the experimental data and the modelling results is shown in Fig.(23)(a,b), for both n=1 B_r sine and cosine components, respectively, together with the corresponding residuals, reported in Fig.(23)(c,d). The agreement, in both the cases, is optimal, as shown by the high value of the *fitpert* parameter and the level of residuals, well below the 10 mV threshold.

The transfer functions between the P1 coils and the n=1 B_r components are:

$$\begin{cases} H_{sin}(s) = -\dfrac{0.32s - 3.40}{s^2 + 91.9s + 2234.07} \\ H_{cos}(s) = -\dfrac{0.05}{s + 57.39} \end{cases} \tag{30}$$

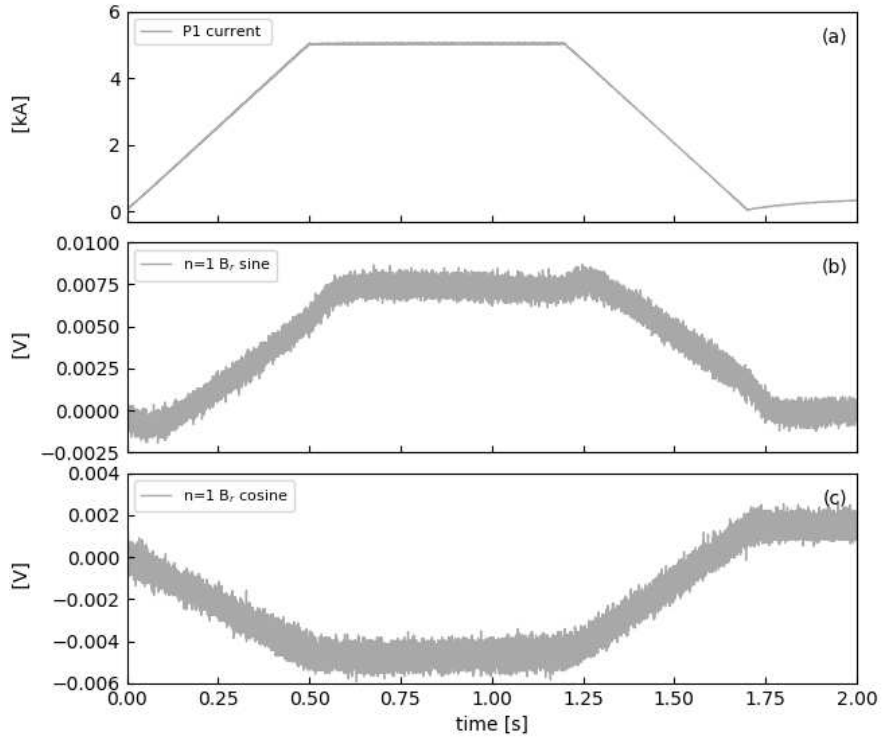

Figure 21: Time behavior of (a) current flowing in P1 coil (b) filtered n=1 B_r sine component (c) filtered n=1 B_r cosine component. Data refers to 43322 vacuum discharge.

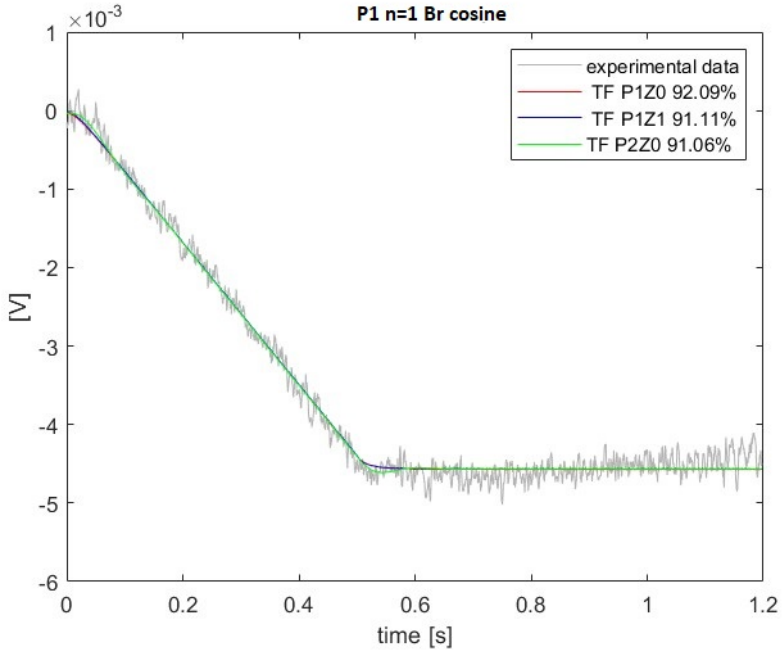

Figure 22: Comparison of the *fitpert* parameter for three models tested for the n=1 B_r cosine component.

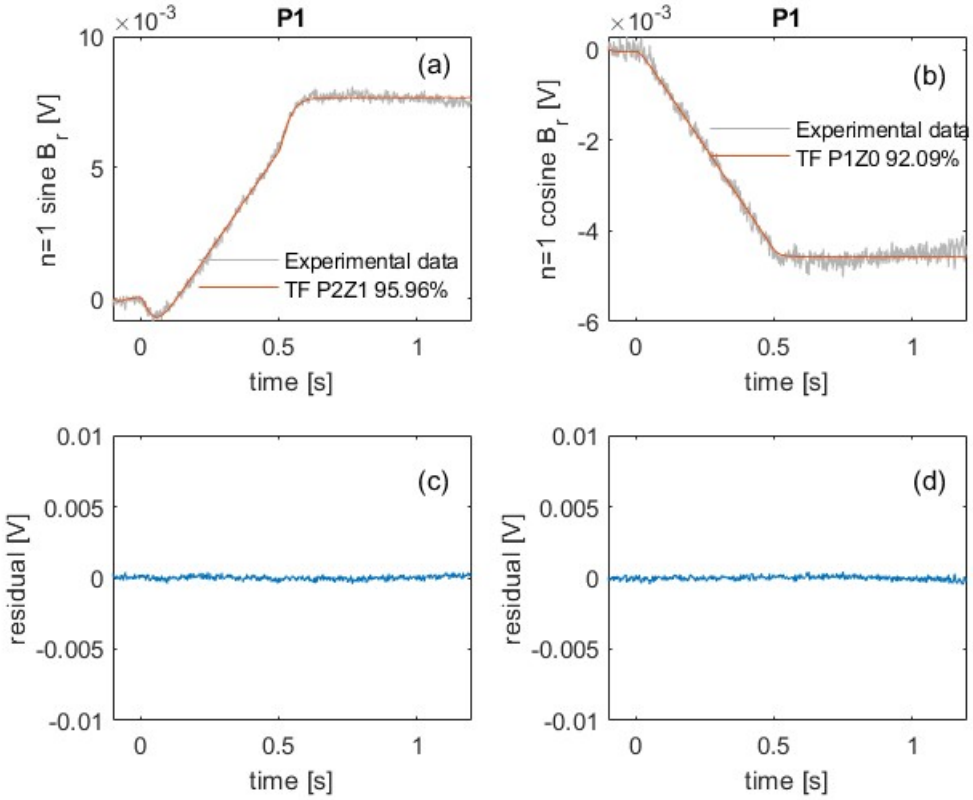

Figure 23: (a) Comparison between the simulated data, using a model with two poles and one zero i.e. P2Z1, and the n=1 B_r sine component. (b) Comparison between the simulated data, using a model with a single pole i.e. P1Z0, and the n=1 B_r cosine component. (c) Residual of n=1 B_r sine w.r.t the simulated data. (d) Residual of n=1 B_r cosine w.r.t the simulated data.

3.1.3 The TF of D6 coil

MAST-U device is equipped with 14 up-down symmetric divertor coils which have been installed during the upgrading phase of MAST machine, to contribute on exhaust studies. The magnetic field topology induced by these coils allow to deposit heat loads on the divertor plates and to flush impurities from the plasma. This procedure is necessary to protect the plasma facing components and to guarantee good plasma performance.

Here, the TF identification among D6 coil, placed in the upper divertor region, and the n=1 B_r components is reported, as an example. The vacuum shot 43831 has been used for this scope. Fig(24(a) shows the time behavior of D6 coil current for this discharge, while the induced n=1 B_r sine and cosine components are reported in Fig.(24(b,c).

As in the previous case, different combinations of poles and zeros have been tested. Fig.(25) shows and example of such a test for n=1 B_r cosine component where three TF models have been reported: P2Z0 in red, P2Z1 in blue and P2Z2 in green. Among them, the optimal model is P2Z2 as suggested from the *fitpert* parameter. Instead, in the case of the n=1 B_r sine component, the best choice is a model with two poles and one zero. In both cases the *fitpert* parameter is above 90%.

The comparison among the experimental data and the modelling results are shown in Fig.(26)(a,b), for the n=1 B_r sine and cosine components, respectively, while the corresponding residuals are reported in Fig.(23)(c,d). The agreement, in both the cases, is optimal as shown by the high value of the *fitpert* parameter and the low level of residuals.

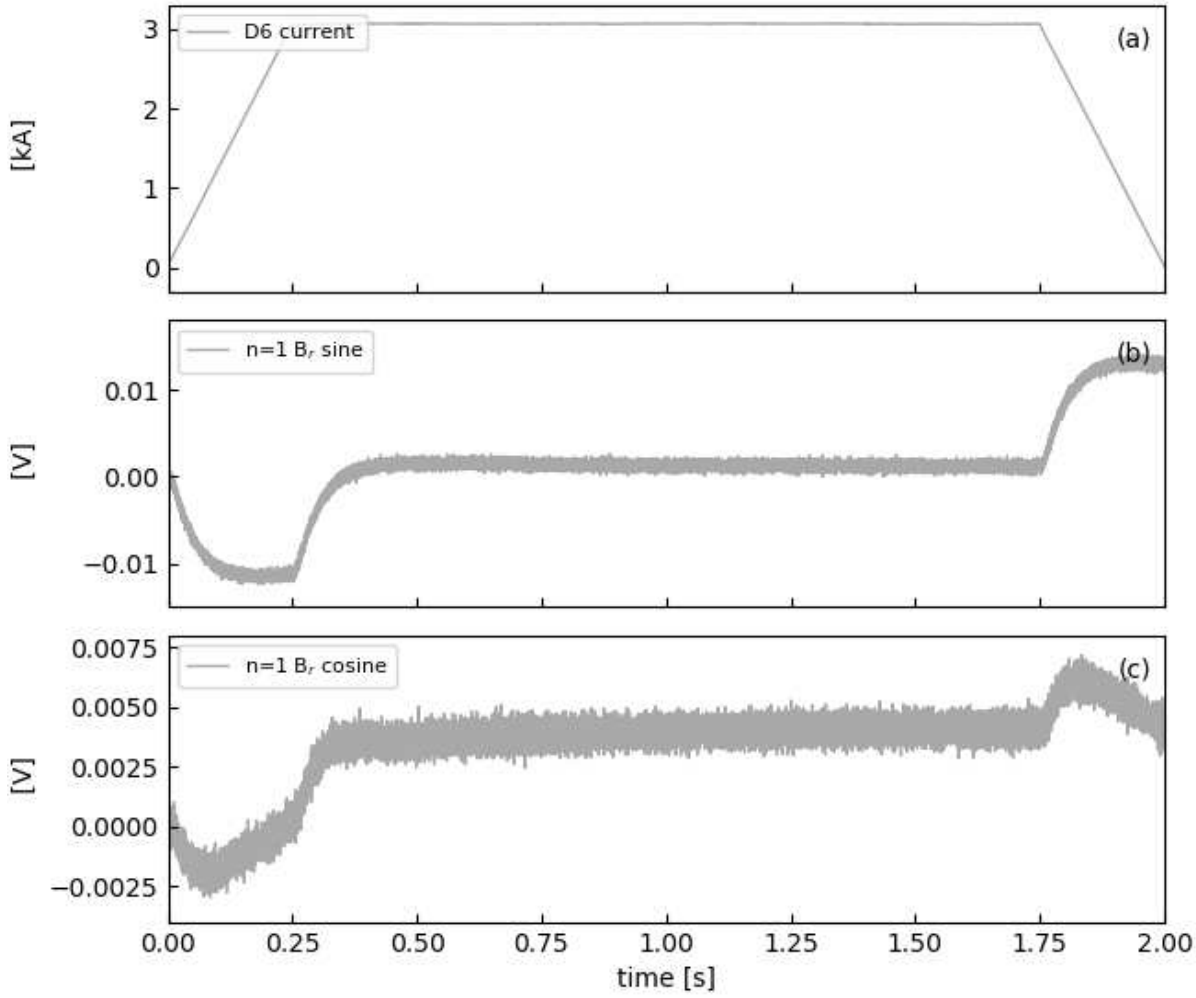

Figure 24: Time behavior of (a) current flowing in D6 coil (b) filtered n=1 B_r sine component and (c) filtered n=1 B_r cosine component. Data refers to 43831 vacuum discharge.

The expressions of the transfer functions estimated for D6 and the n=1 B_r sine and cosine components are:

$$\begin{cases} H_{sin}(s) = -\dfrac{2.07s - 0.86}{s^2 + 105.59s + 2062.10} \\ H_{cos}(s) = -\dfrac{0.006s^2 - 0.022s - 0.04}{s^2 + 28.87 + 32.04} \end{cases} \tag{31}$$

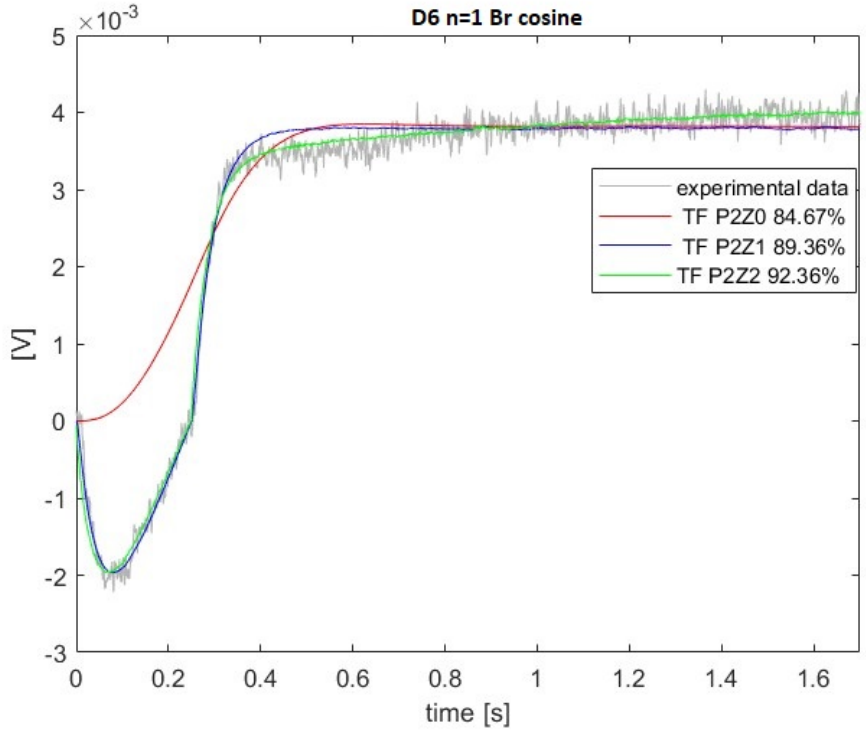

Figure 25: Comparison of the *fitpert* parameter for three model tested for the n=1 B_r cosine component i.e. P2Z0 in red, P2Z1 in blue and P2Z2 in green. The best choice in this case is the model P2Z2.

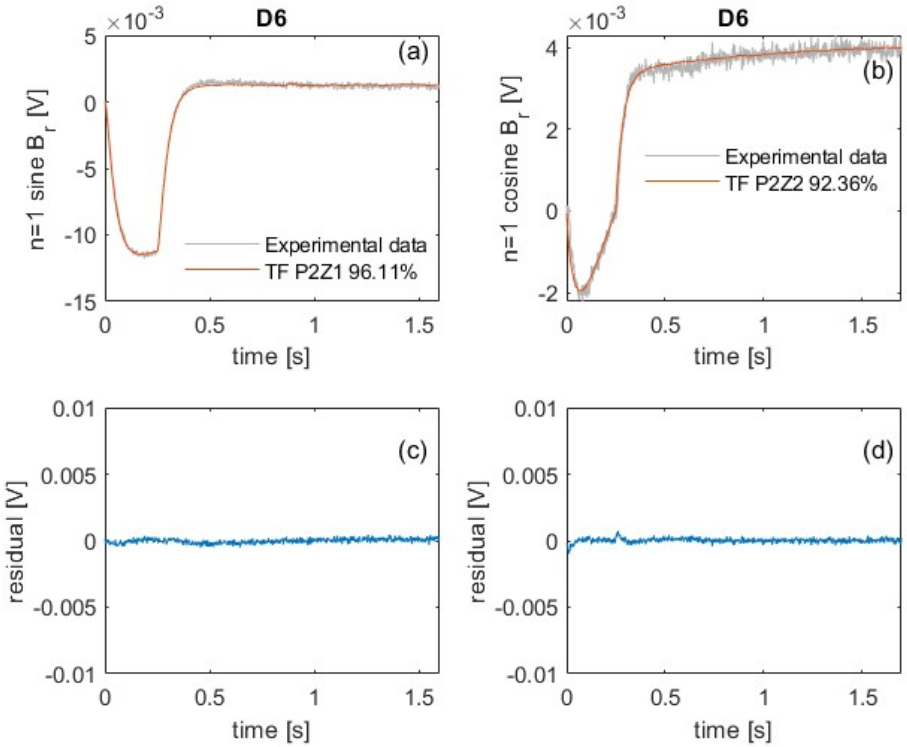

Figure 26: (a) Comparison between the simulated data, using a model with two poles and one zero i.e. P2Z1, and the n=1 B_r sine component. (b) Comparison between the simulated data, using a model with two poles and two zeros i.e. P2Z2, and the n=1 B_r cosine component. (c) Residual of n=1 B_r sine w.r.t the simulated data. (d) Residual of n=1 B_r cosine w.r.t the simulated data.

4 Error field identification

In this chapter, the methodology described previously that allows the calculation of the vacuum external magnetic field is applied to plasma discharges. In particular, the total magnetic field is compensated by the vacuum external field, allowing the study of the plasma response behavior and the identification of the time instant of the locked mode onset. Such an analysis permits to resolve empirically the correction currents for error field minimization, and to assess possible dependence of locked mode onset with plasma parameters.

4.1 The compass scan

During the execution of the compass scan method, as described in chapter 1, the EFCC power supplies are connected in $n = 1$ configuration and a current ramp up is pre-programmed, while varying the toroidal phase. The aim is to apply an external error field able to trigger a locked mode.

Due to the presence of the machine's intrinsic error field, the current required to form a locked mode varies with the phase of the externally applied magnetic field. A certain phase of the external field will add to the intrinsic error field, while the opposite phase will oppose the intrinsic error field.

The locked mode onset currents, as the external field is ramped with several different toroidal phases, lay on a circle whose center can be identified. Its possible offset from the starting point

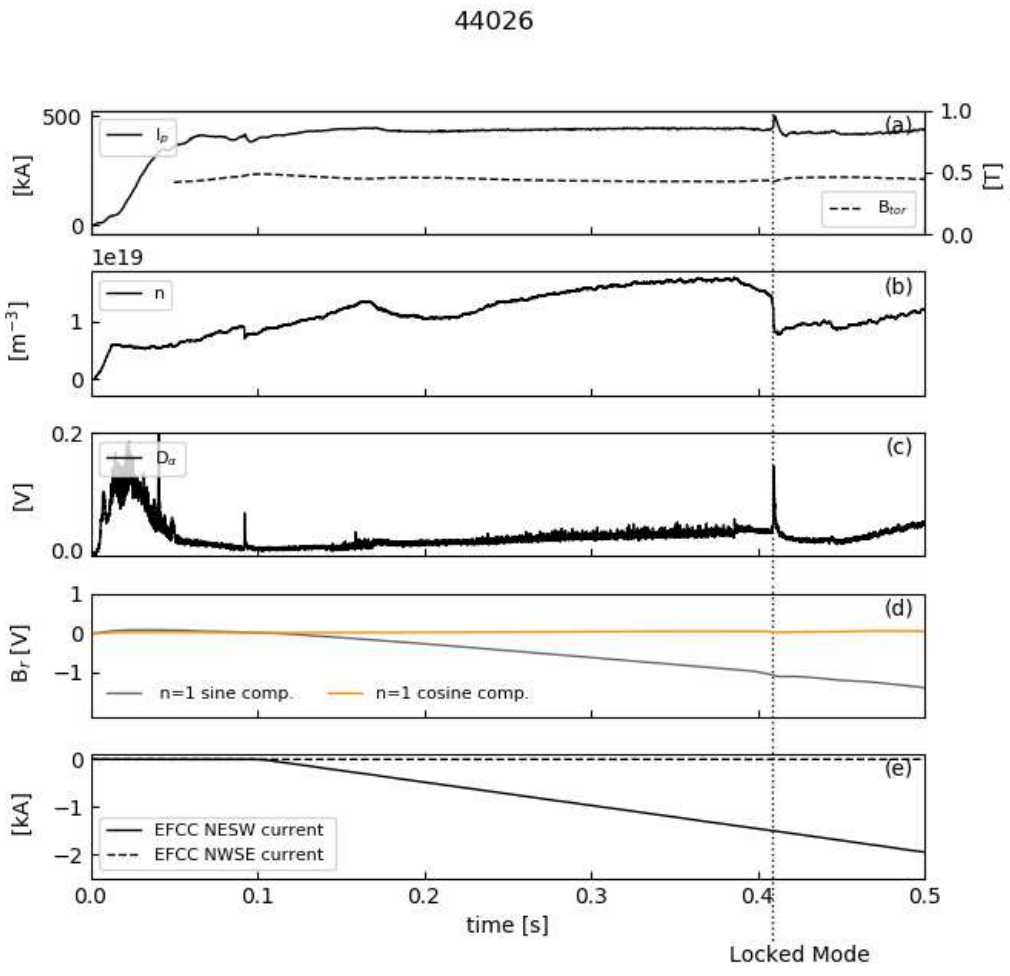

Figure 27: Time behavior of a) plasma current and toroidal magnetic field on axis, b) plasma density, c) D_α emission, d) n=1 radial magnetic field components and e) EFCC currents. Data refers to 44026 discharge.

of the current ramps yields the coil correction currents needed to minimize the intrinsic error field.

The compass scan method has been used in MAST-U to identify the $n = 1$ error field source. In this Thesis work, a database of 90 discharges, where the compass scan has been executed, have been analyzed considering data from multiple diagnostics. These experiments have been performed in 2021 in the framework of EUROFusion Reseach Topic 1 [50].

The study of n=1 error field identification has been carried out in an Ohmic plasma scenario with plasma current I_p=400 kA, and three values of toroidal magnetic field current, I_{TF} = 74, 79 and 89 kA. When executing the compass scan, the EFCC current has been increased up to 2.5 kA, the maximum current level achievable with the present available power supplies.

An example of compass scan test is reported in Fig.(27), and refers to a 400 kA plasma current, 0.4 T toroidal magnetic field discharge. The current in the EFCCs is ramped up from t=0.1 s, using just one pair of EFCCs, named NESW, as shown in Fig.(27)(e). The compass scan is executed during the plasma current flat-top phase, in order to avoid spurious effects, as the ones introduced by the eddy currents. The evolution of plasma density is dictated, in this first MAST-U campaign, by a mid-plane gas valve opening, which has been adjusted in feed-forward. Unfortunately, a density control scheme acting in real-time was not available in this early campaign. This justifies why the density is not kept constant, but has some dynamics, as reported in Fig.(27)(b).

Consistently with the experimental evidences observed in JET [51] and in DIII-D [52], when

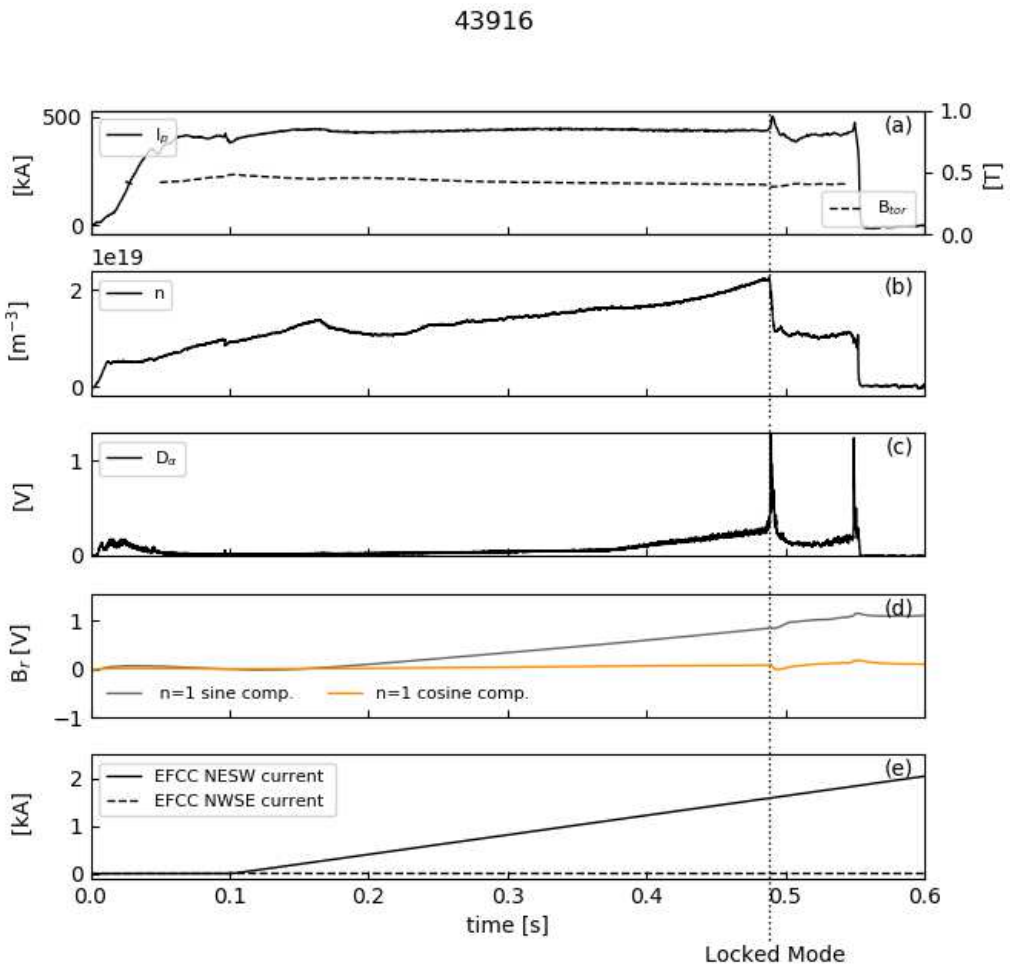

Figure 28: Time behavior of a) plasma current and toroidal magnetic field on axis, b) plasma density, c) D_α emission, d) n=1 radial magnetic field components and e) EFCC currents. Data refers to 43916 discharge.

the field penetration occurs, which corresponds to the locked mode triggering, its signature can be detected as a growing n=1 radial magnetic field perturbation on the saddle coils data, as shown in Fig.(27)(d), accompanied by a drop in the plasma density and an increase in the D_α emission, as shown in Fig.(27)(b) and Fig.(27(c), respectively. In the same figure, the time instant of field penetration is indicated with a dotted line.

The occurrence of the field penetration can be straightforward detected in some discharges, as the one shown in Fig.(28), where an evident imprint on the total magnetic field component can be seen in Fig.(28)(d). However, for the majority of the discharges analyzed, the detection of the field penetration would be not so simple, as the case presented in Fig.(29).

This motivates the development of a robust and reliable tool able to detect when the field penetration process occurs. The instant of field penetration has been detected considering the following procedure:

1. Calculation of the external magnetic field, using the methodology described in the previous chapter;

2. Compensation of the total magnetic field from the external one, thus obtaining the plasma response;

3. Detection of the time instant of field penetration whose signature corresponds to an abrupt change in the first derivative of the plasma response signal.

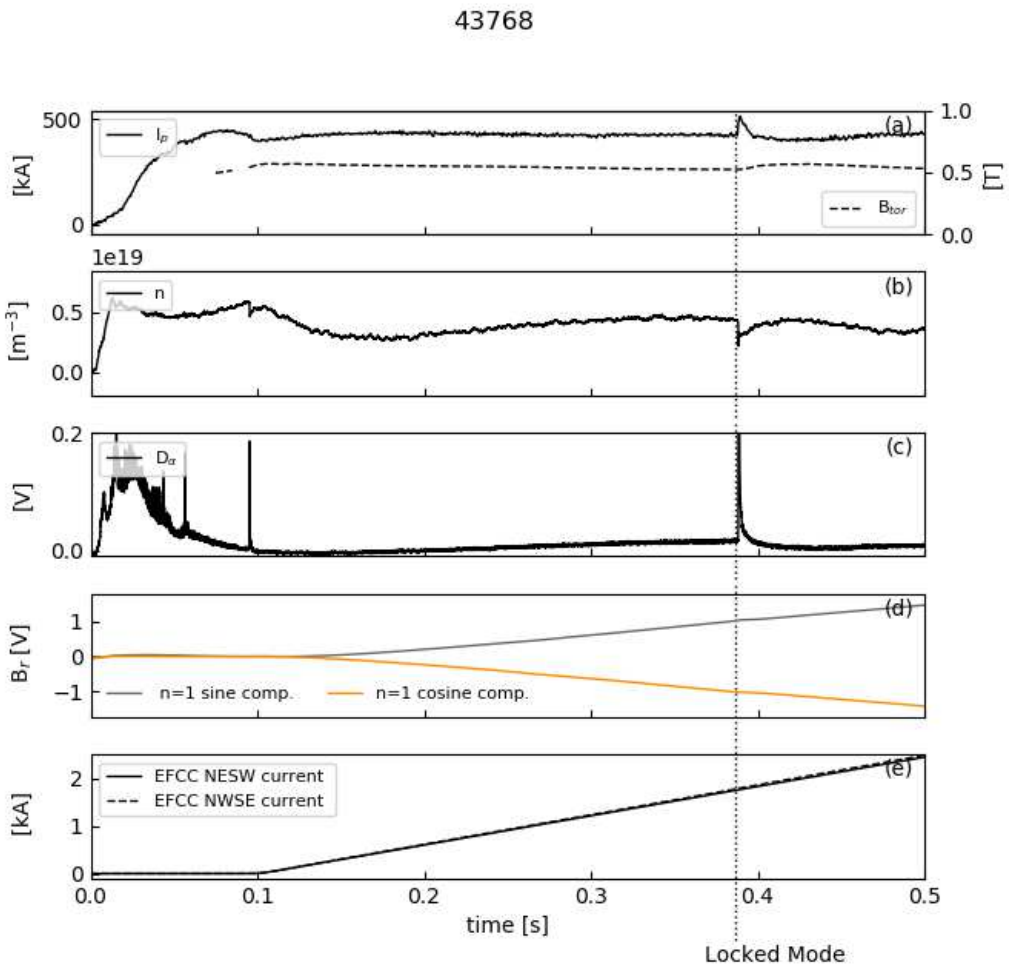

Figure 29: Time behavior of a) plasma current and toroidal magnetic field on axis, b) plasma density, c) D_α emission, d) n=1 radial magnetic field components and e) EFCC currents. Data refers to 43768 discharge.

Such a procedure has been implemented in a MATLAB code and applied for each discharge of the database. The detection of the field penetration used magnetic signals but has been also corroborated considering evidences in D_α and density measurements. The identified instants of field penetration were then stored and used to calculate the correction currents for error field minimization, as described in subsection 4.3.

Fig.(30) shows the results of the previous procedure applied to discharges 43916 and 43768, which are an easy and difficult example of field penetration detection, respectively.

In particular, panels (a,b) of Fig.(30) show the time evolution of the sine and cosine components of the total n=1 radial magnetic field, as deduced by saddle coils signals using the formula reported in subsection 3.1. Panels (c,d) of Fig.(30) report the sine and cosine components of the external n=1 magnetic field. These components have been calculated using the matrix $M(\omega)$ and the actuator's currents for every shot, as described in section 3.

The difference among the n=1 components of B_{tot} and B_{ext} allows the calculation of the

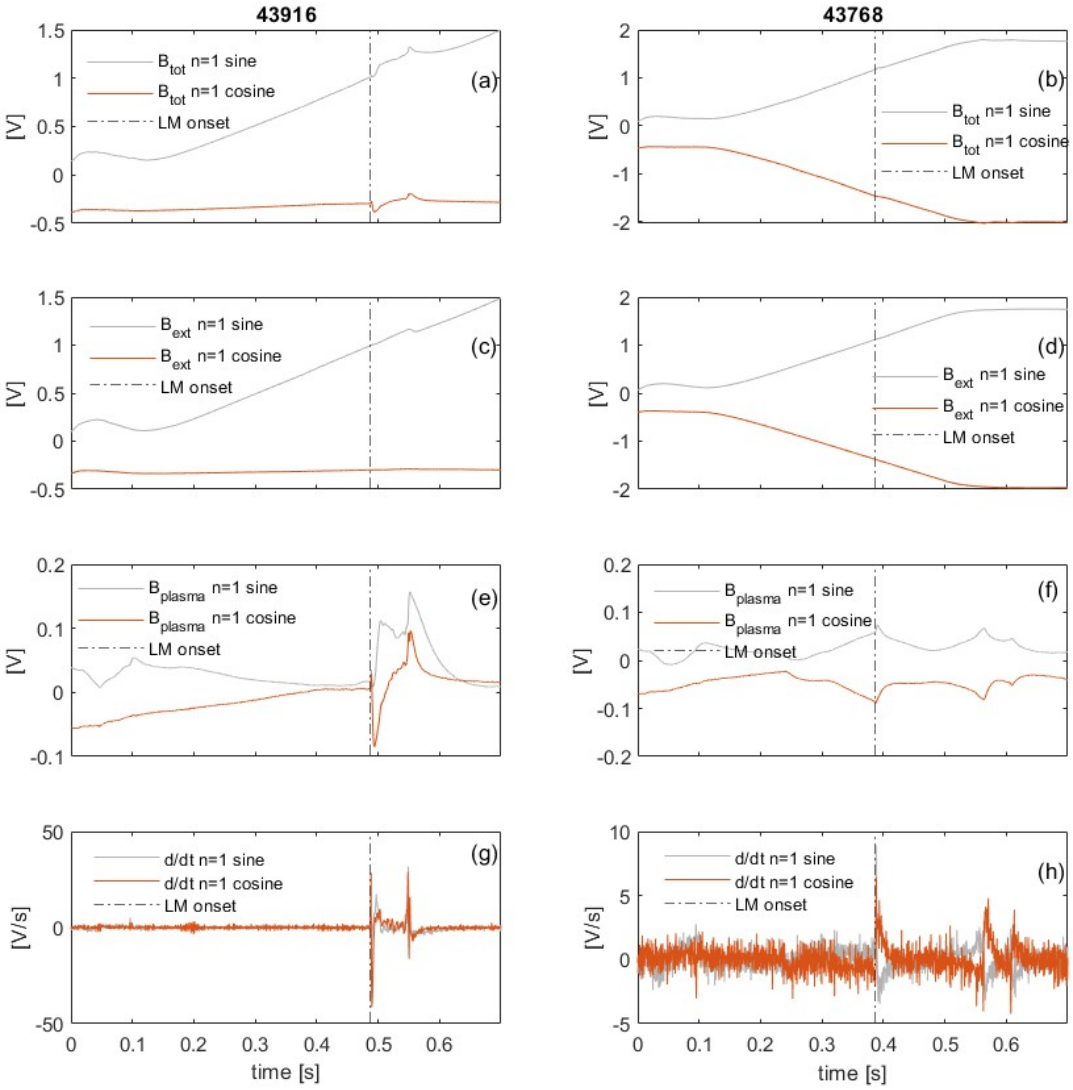

Figure 30: Time behaviour of (a,b) total n=1 radial magnetic field components, i.e. B_{tot}, (c,d) modelled external n=1 radial magnetic field components, i.e. B_{ext}, (e,f) plasma response, namely the difference between B_{tot} and B_{ext}, (g,h) time derivative of the plasma response. Data refers to discharges 43916 (on the left) and 43768 (on the right).

plasma response, reported in panels (e,f) of Fig.(30). This quantity is of primary interest since it describes the evolution of the MHD activity, which in these Ohmic plasmas corresponds to the locked mode dynamics.

As previously anticipated, to detect the time of field penetration, the first time derivative of the plasma response has been calculated. Fig.(30)(g,h) represent such quantity. Note that specially for discharge 43768, the identification of the field penetration becomes much clearer utilizing the methodology just described. Indeed, as shown in Fig.(30)(h), the time derivative of plasma response reveals straightforwardly the time of the field penetration.

4.2 Evidence of locked mode onset scaling with density

It is well documented in literature, considering results from various devices, such as JET, C-mod and DIII-D [51] and the previous MAST machine [3], that the scaling law of the locked mode onset with density is linear. To assess if a similar result is valid also for MAST-U, the discharges have been divided in ensembles according to the current flowing in the central solenoid.

In order to observe a possible dependence of the locked mode onset as a function of the density, it is necessary to convert the line density n_l from interferometer diagnostics (see subsection 2.3), into volume density (number of particles per unit volume). This calculation can be performed considering the length of the chord of the interferometer. The chord length depends on the plasma shape and must be calculated for each shot separately.

Let r_{in} and r_{out} be respectively the inner and outer plasma radius on the midplane and r_{tan} the tangency radius of the interferometer chord, outcomes of EFIT++ calculation. The volume density is obtained applying the following formula:

$$n = \frac{n_l}{\langle 4\left[\sqrt{r_{in}^2 - r_{tan}^2} - \sqrt{r_{out}^2 - r_{tan}^2}\right]\rangle} \tag{32}$$

where the average of the denominator has been calculated on a time interval where the line density profile was flat. This formula has been applied to every shot of the database to retrieve the volume averaged density.

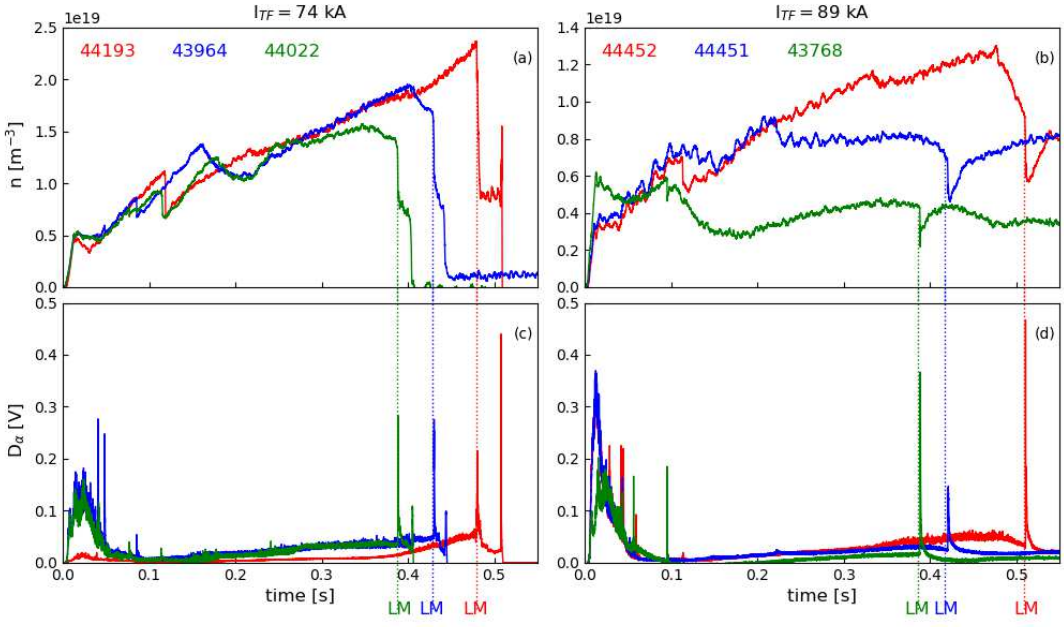

Figure 31: Time behaviour of (a,b) volume averaged density and (c,d) D_α for two sets of discharges with various densities and two values of I_{TF}, 74 and 89 kA, on the left and on the right, respectively.

Fig.(31) shows the time behavior of volume average density and D_α signals in discharges with two values of I_{TF}, 74 and 89 kA, on the left and on the right, respectively. The color code has been used to distinguish the various shots analyzed. Note that the onset of the locked mode is delayed in plasmas with higher densities in both the ensamble of discharges presented.

This confirms the expected trend, which is consistent with previously results obtained in MAST device [3] and in other tokamaks.

In future, to investigate further possible dependencies of the locked mode onset on the main plasma parameters, such as plasma current, electron temperature and plasma rotation, dedicated experiments will be performed in the 2022 MAST-U campaign.

4.3 Error field correction currents

The analysis carried out, besides showing a delay in the locked mode onset with plasma density, allows also to deduce the error field correction currents. To calculate such quantities, the following procedure has been adopted:

1. Select, from the database of discharges analyzed, at least four shots with different phase of the external field, with approximately the same density and with the same I_{TF};

2. Report in a polar plot the EFCC currents at the time instant of the field penetration;

3. Fit the values with a circle, whose center represents the error field correction currents.

If the device does not have any intrinsic error field, the center of the circle would lie on the origin of the axis, meaning that no correction is needed. Otherwise, the possible offset from the origin suggests the presence of an intrinsic error field and yields the inferred coil currents for error field compensation.

Fig.(32) and Fig.(33) show the results of the compass scan method. In particular, Fig.(32) represents the compass scan obtained considering plasmas with density in the range n = 1.3-1.6$\times 10^{19}$ m^{-3} and $I_{TF} \approx 74$ kA. Fig.(33) represents the same results, but considering plasmas with density in the range n = 0.5-1.0$\times 10^{19}$ m^{-3} and $I_{TF} \approx 89$ kA. It is worth highlighting that no results of the compass scan for plasmas with $I_{TF} \approx 79$ kA have been reported being the procedure above mentioned not applicable. Indeed, two discharges only are available at this level of I_{TF}, which are not enough to deduce the empirical correction currents.

Note that in both the compass scans presented, the center of the circle is slightly shifted upwards, so a n=1 error field is present. For the plasmas with $I_{TF} \approx 74$ kA, the deduced correction currents are (EFCC NESW, EFCC NWSE)= (-0.0006 $\pm$ 0.01, 0.10 $\pm$ 0.02) kA, While, for the plasmas with $I_{TF} \approx 89$ kA, the correction currents correspond to (EFCC NESW, EFCC NWSE)= (0.009 $\pm$ 0.02, 0.22 $\pm$ 0.04) kA.

The deduced correction currents for error field minimization are rather small, a promising indication of a small error field. The compass scan method performed in MAST device yielded error field correction currents of the order of kA [42]. Having obtained in MAST-U correction currents of few hundreds of amperes is a positive result. This proves that the fine tuning of coil installation when assembling MAST-U device to compensate the n=1 intrinsic error field has been a successful strategy [1].

In summary, the method developed in section 3 proved to be a reliable tool to detect the locked mode formation which allows to i) observe a linear trend of the locked mode onset with density and ii) draw the conclusion that the n=1 error field source for this plasma scenario is small.

It is worth mentioning that the compass scan has been partially executed in some configurations. For example, EFCC NESW = 0 kA and EFCC NWSE > 0 kA are missing in

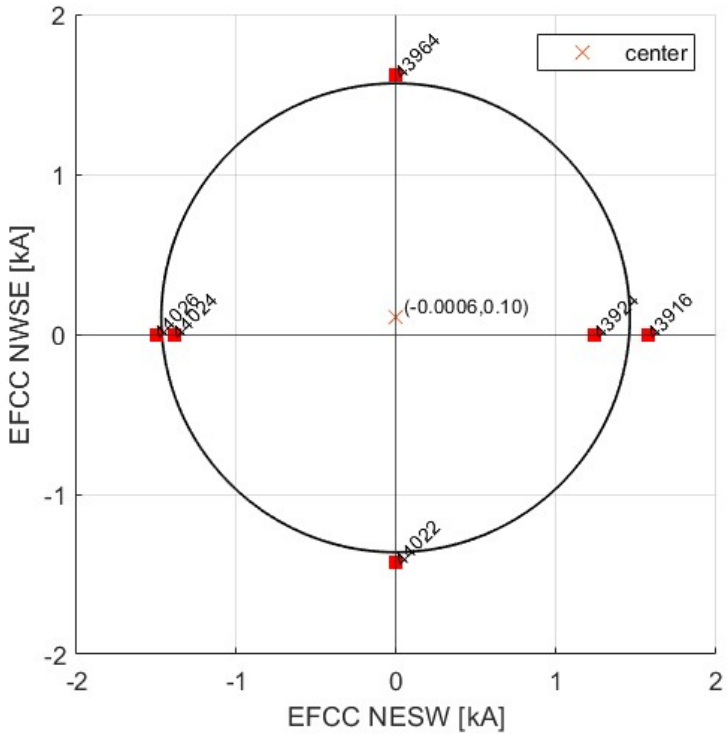

Figure 32: Compass scan in 400 kA plasma current, $I_{TF} \approx 74$ kA and density n = 1.3-1.6×10^{19} m^{-3} plasmas. The optimal error field correction current are resolved fitting a circle to data. The center is located at (-0.0006 ± 0.01, 0.10 ± 0.02) kA.

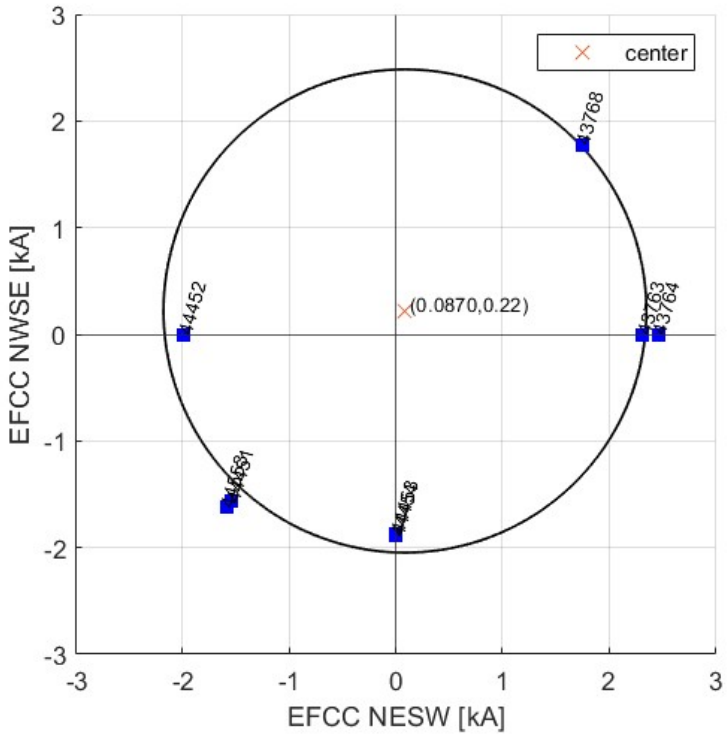

Figure 33: Compass scan in 400 kA plasma current, $I_{TF} \approx 89$ kA and density n =0.5-1×10^{19} m^{-3} plasmas. The optimal error field correction current are resolved fitting a circle to data. The center is located at (0.009 ± 0.02, 0.22 ± 0.04) kA.

the ensamble of discharges with $I_{TF} \approx 89$ kA. Dedicated experiments are planned in the next MAST-U campaign to fill this gap and to reinforce the results obtained.

The algorithm developed to identify the locked mode onset based on signal compensation and first derivative of the plasma response signal shows to be a robust procedure over the whole database. Its reliability in detecting the locked mode onset will be exploited in near future for real time applications in MAST-U, such as disruption avoidance, and potentially, thanks to its portability, it can be also applied to other fusion devices.

5 Conclusions

This Thesis work focuses on the identification of the n=1 intrinsic error field source in MAST-U device, which is based on the original MAST machine, but recently upgraded to enable the exploration of high plasma performance scenarios and to contribute on plasma exhaust physics.

The study presented here is of relevant importance since the presence of error fields, spurious magnetic field perturbations, can inhibit the achievements of these targets. Indeed, error fields can i) trigger MHD instabilities, ii) induce fast ion losses, iii) brake plasma rotation, iv) degrade plasma performance, and v) in more severe cases, be responsible of plasma disruptions and thus damage the machine integrity. Because of these effects, a dedicated experimental campaign has been performed at the beginning of MAST-U operation, in 2021, to identify the n=1 error field source. This study has been carried out in the framework of FP9 Horizon program, WorkPackage Tokamak Exploitation RT01: ITER baseline scenario towards detachment and low collisionality.

The method applied for error field identification is the compass scan technique, described in section 1. Such a method has been executed in 90 discharges, which have been analyzed statistically considering data from multiple diagnostics, such as signals of magnetic field fluctuations, density and D_{alpha}. To identify the error field, the compass scan relies on the detection of the field penetration, which is the process by which a locked mode forms. Hence, it is of paramount importance to detect, by means of a robust and a reliable methodology, such a time instant.

To this aim, a sophisticated tool has been developed. Such a tool is based on the transfer function identification among each actuator (divertor, poloidal, toroidal field and error field correction coils) and the n=1 radial magnetic components. The transfer function allows the calculation of the external magnetic field, which is the contribution that needs to be subtracted from the total radial magnetic field, thus providing the estimation of the plasma response.

The plasma response is a key quantity for this study since it provides information on the dynamics of MHD modes present in the plasma analyzed, i.e. locked mode behavior. By analyzing the plasma response evolution, and in particular, by seeking an abrupt change in the slope of this signal, automatically detected considering its time derivative, the time of field penetration, or locked mode formation, can be correctly estimated.

Such information, deduced by magnetic data only, has been also complimented with other signals such as D_α and density measurements, which contain signature of this process.

This procedure has been applied to the database of discharges aforementioned, allowing the fulfilment of the two objectives of this Thesis:

- Identify the n=1 error field. By executing the compass scan, the correction currents, which allow n=1 error field minimization, have been deduced in 400 kA plasma current plasma scenario with two levels of toroidal field current: 74 kA and 89 kA. In MAST-U, the correction currents are of the order of hundreds of Ampere, significantly smaller than the ones deduced in MAST, in the kilo Ampere range. This suggests that the intrinsic error field is small in MAST-U and an homeopathic level of correction current is needed for its minimization. This result demonstrates that the optimal coil alignment adopted when assembly MAST-U to minimize the intrinsic n=1 error field has been a successful strategy [1].
- Assessing the linear dependence of the locked mode formations as a function of the density. The linear dependence has been demonstrated, consistently with previous studies performed in MAST and in other devices, such as DIII-D and JET.

The methodology developed in this Thesis work to identify the locked mode onset, based on signal compensation and first derivative of the plasma response signal, shows to be a robust

procedure over the whole database. Its reliability in detecting the locked mode onset will be exploited in near future for real time applications in MAST-U, such as prediction avoidance. Thanks to its portability, this methodology could be applied also to other fusion devices.

The next steps of this Thesis work aim at further investigating error field detection methods in other fusion devices, such as AUG (Garching, Germany), JET (Oxfordshire, UK), and DIII-D (San Diego, USA), which are equipped with an extensive set of magnetic field sensors and an advanced active system for error field control. The knowledge acquired on this field will be used to develop error field identification methods for near future devices, such as the Divertor Test Tokamak. The error field studies will be also complimented by plasma response modelling, provided by MHD codes, as MARS-F [53] and GPEC [54], to deduce model-based error field control strategies.

6 Appendix

In this chapter, for completeness, the time behavior of the current in the EFCCs NESW, poloidal, divertor and toroidal field coils and the n=1 radial magnetic field components are reported for each vacuum shot used for the TF identification.

Fig.(46) and Fig.(47) show in a compact form the comparison between the experimental data and the TF modelling results.

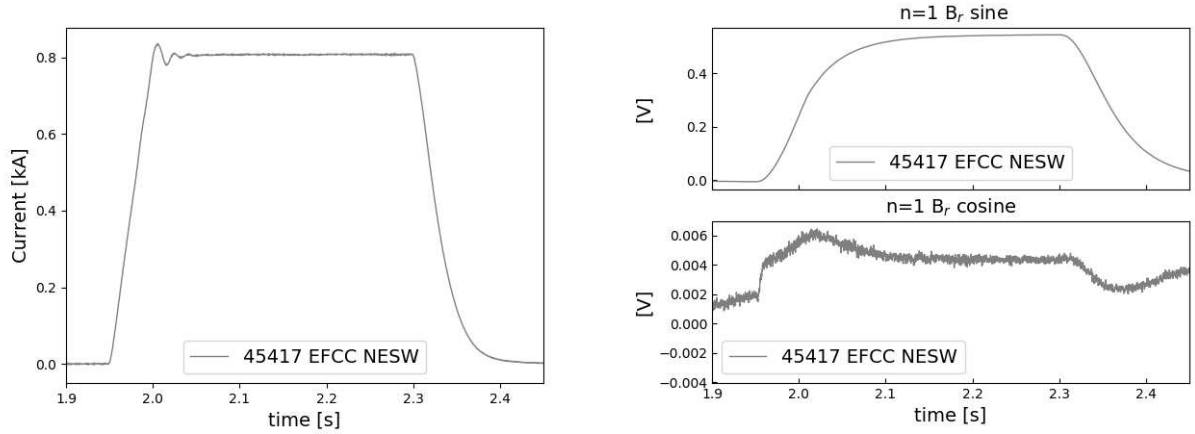

(a) (b)

Figure 34: Time behaviour of (a) current flowing in the EFCCs NESW coils, (b) filtered n=1 B_r sine and cosine.

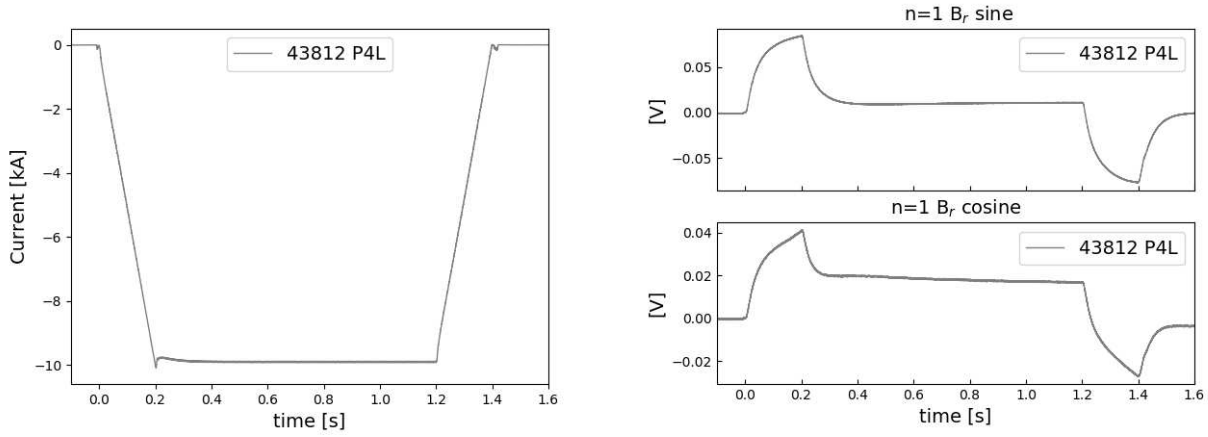

(a) (b)

Figure 35: Time behaviour of (a) current flowing in the P4 coil, (b) filtered n=1 B_r sine and cosine.

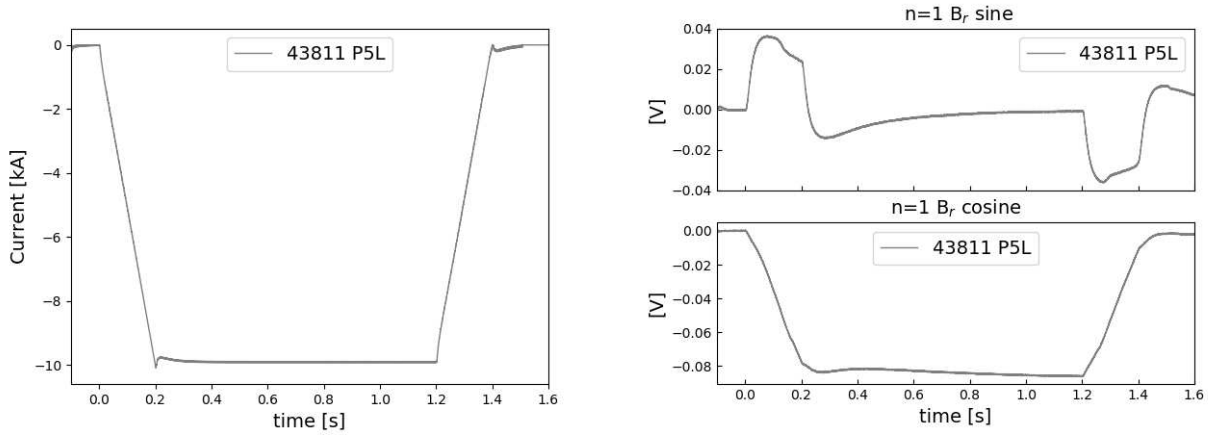

(a) (b)

Figure 36: Time behaviour of (a) current flowing in the P5 coil, (b) filtered n=1 B_r sine and cosine.

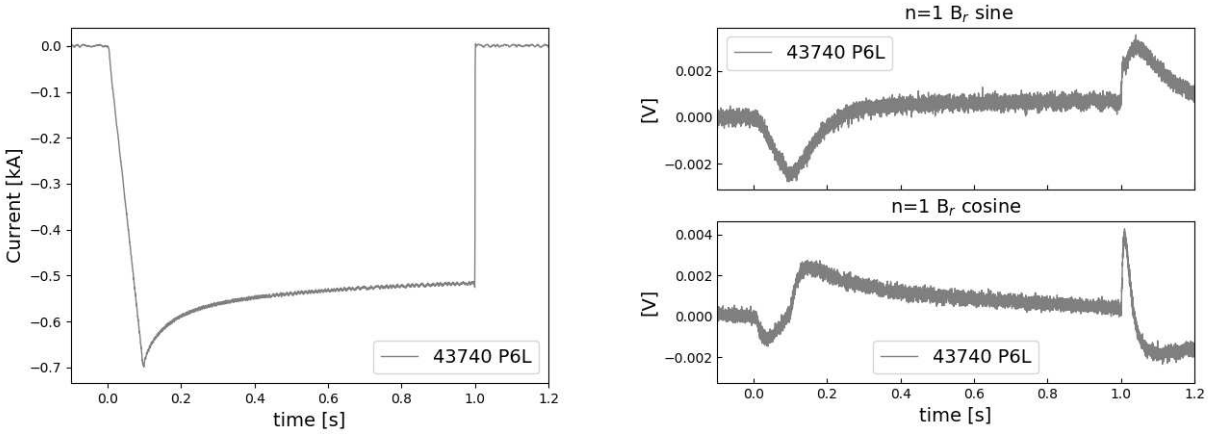

(a) (b)

Figure 37: Time behaviour of (a) current flowing in the P6 coil, (b) filtered n=1 B_r sine and cosine.

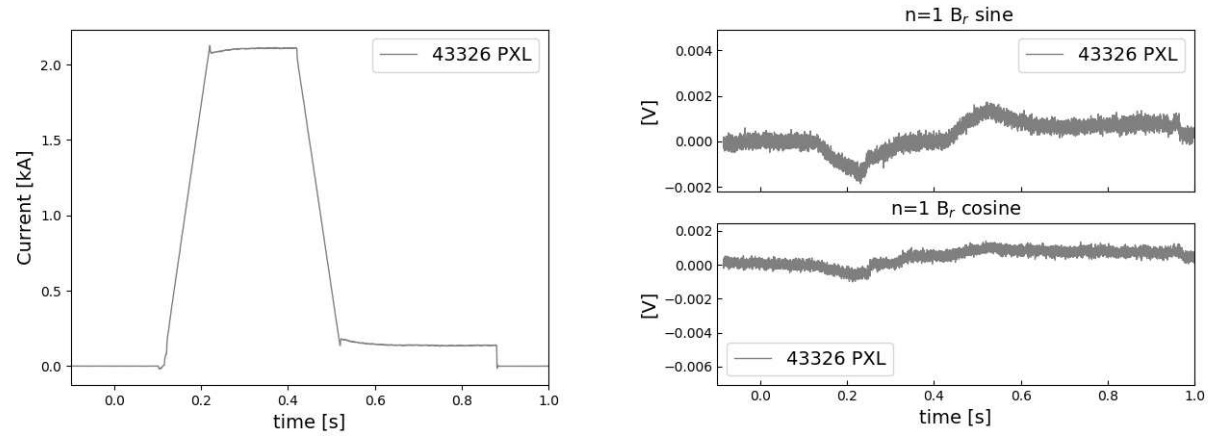

(a) (b)

Figure 38: Time behaviour of (a) current flowing in the PX coil, (b) filtered n=1 B_r sine and cosine.

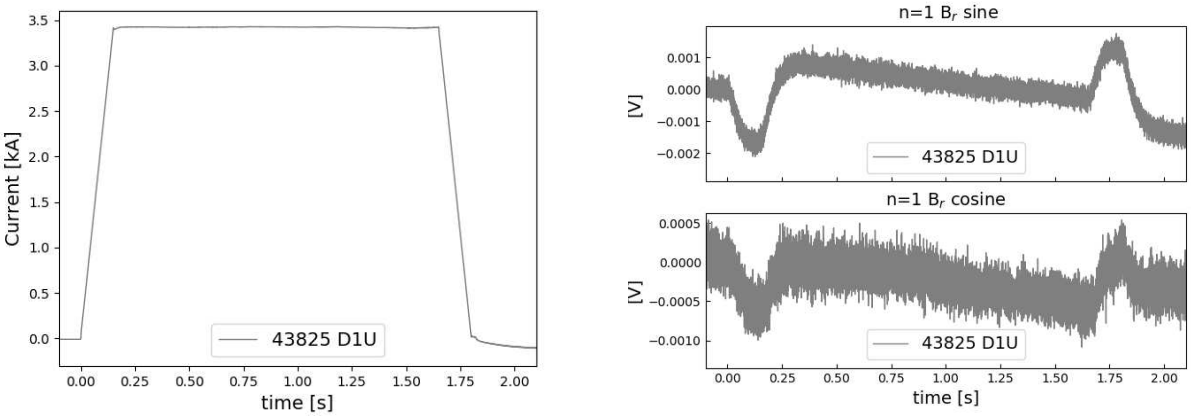

(a) (b)

Figure 39: Time behaviour of (a) current flowing in the D1 coil, (b) filtered n=1 B_r sine and cosine.

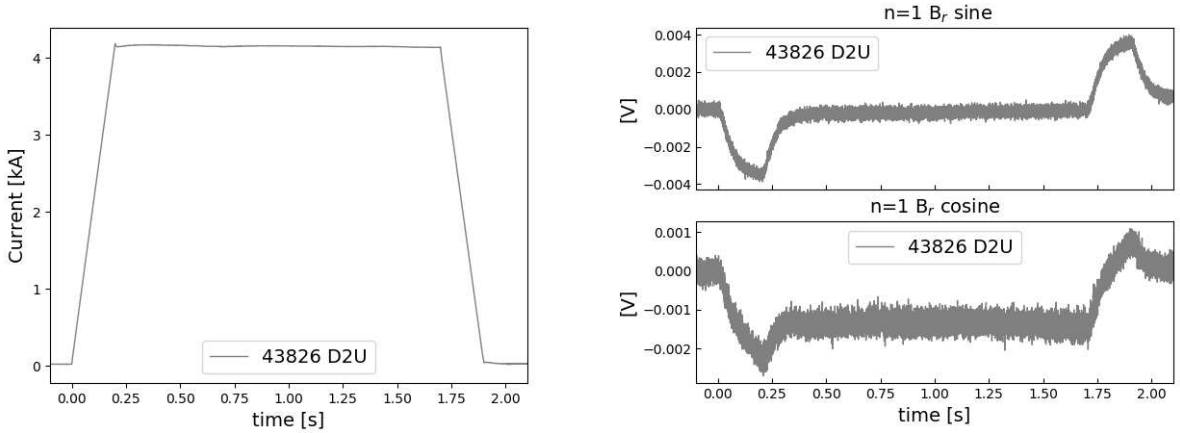

(a) (b)

Figure 40: Time behaviour of (a) current flowing in the D2 coil, (b) filtered n=1 B_r sine and cosine.

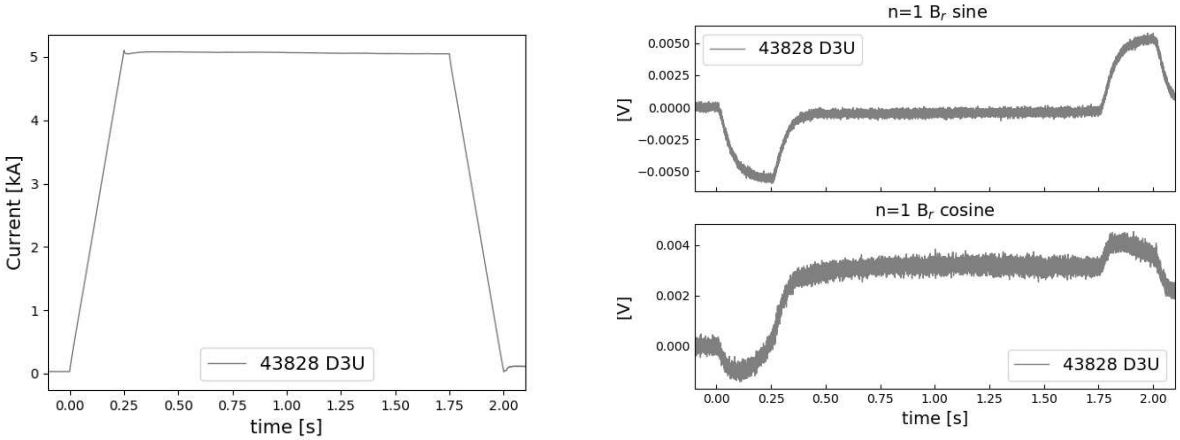

(a) (b)

Figure 41: Time behaviour of (a) current flowing in the D3 coil, (b) filtered n=1 B_r sine and cosine.

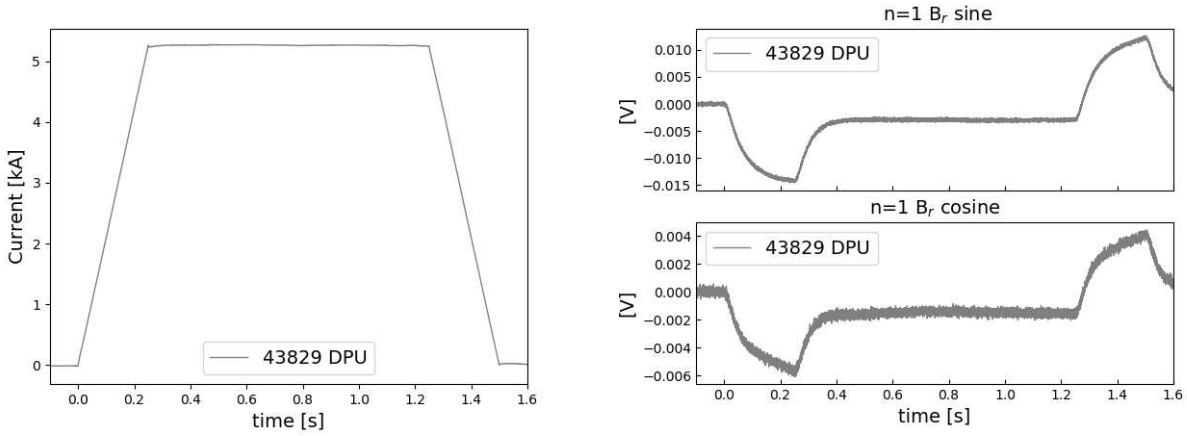

(a) (b)

Figure 42: Time behaviour of (a) current flowing in the DP coil, (b) filtered n=1 B_r sine and cosine.

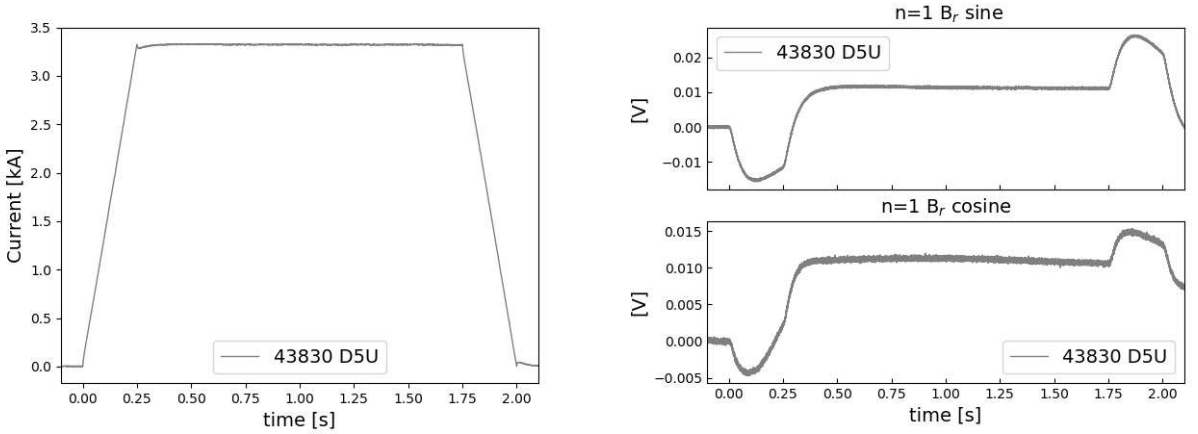

(a) (b)

Figure 43: Time behaviour of (a) current flowing in the D5 coil, (b) filtered n=1 B_r sine and cosine.

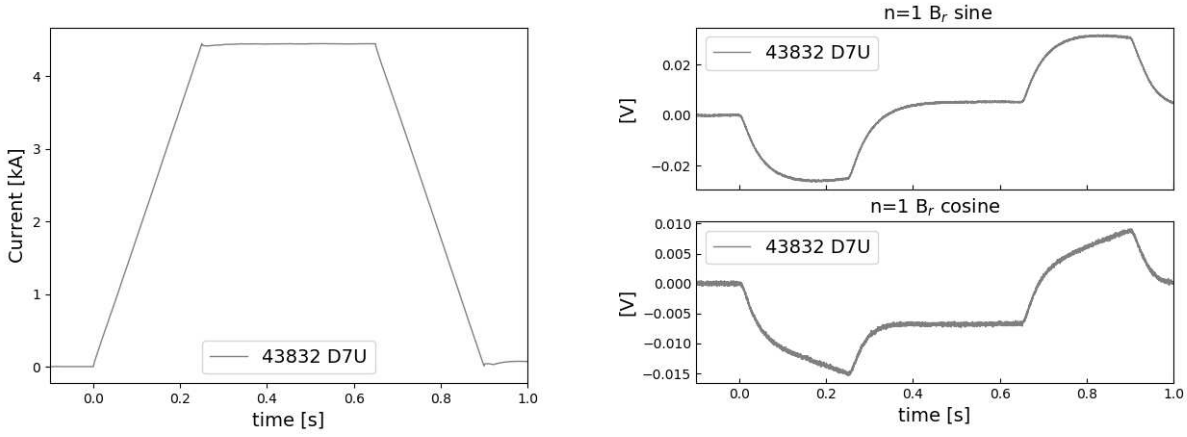

(a) (b)

Figure 44: Time behaviour of (a) current flowing in the D7 coil, (b) filtered n=1 B_r sine and cosine.

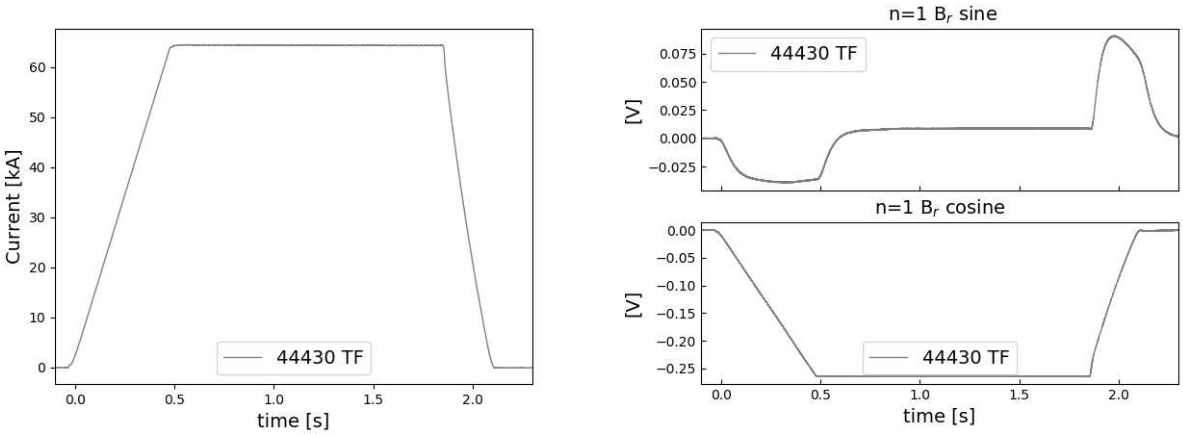

(a) (b)

Figure 45: Time behaviour of (a) current flowing in the TF coil, (b) filtered n=1 B_r sine and cosine.

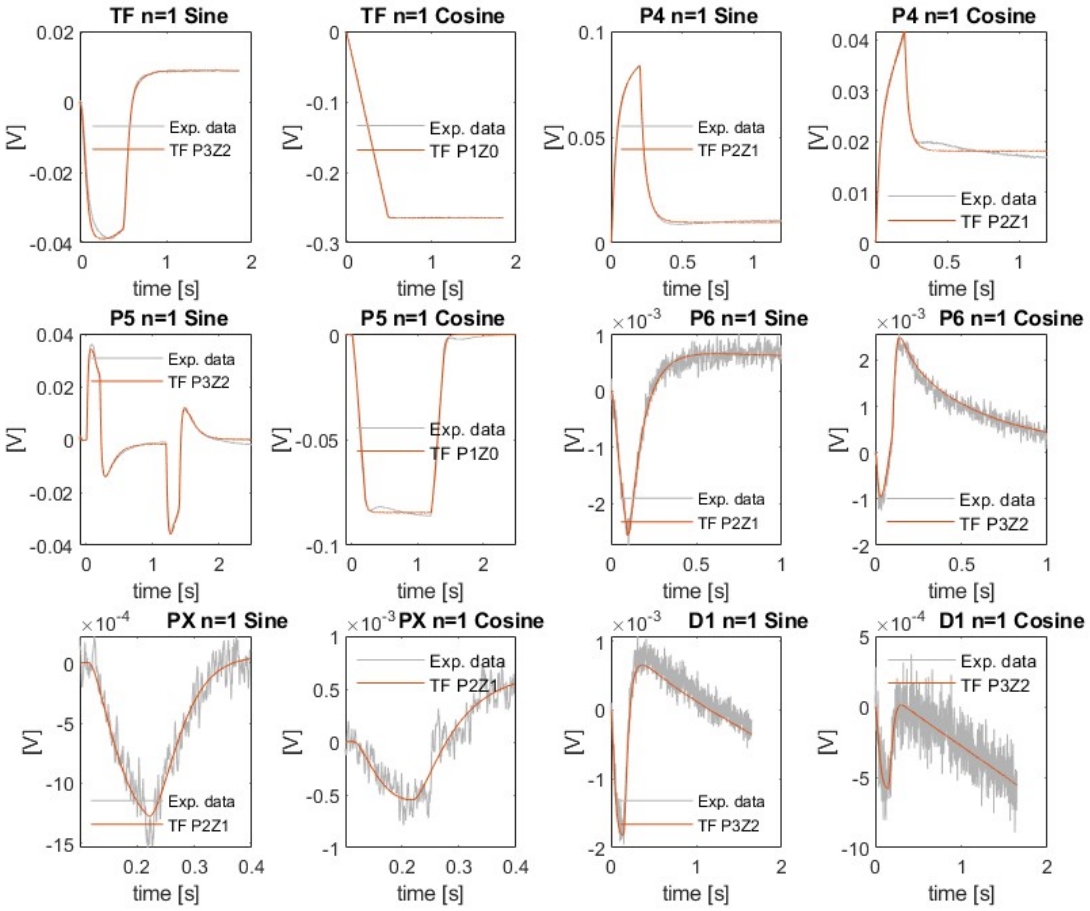

Figure 46: Transfer function identification for both n=1 B_r components of TF, P4 ,P5, P6, PX and D1 coils.

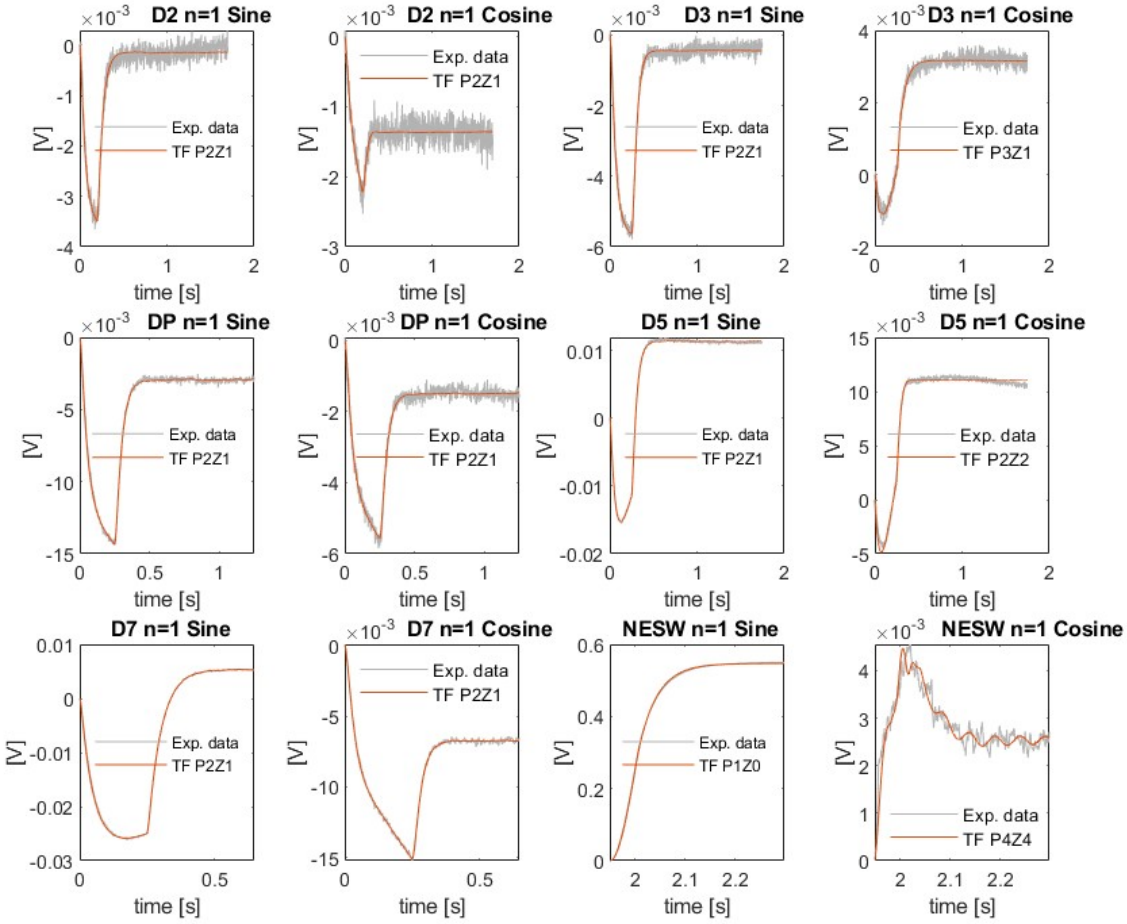

Figure 47: Transfer function identification for both n=1 B_r components of D2, D3, DP, D5, D7, EFCC NESW coils.

7 Bibliography

Articles

[1] L. Piron et al. "Error field correction strategies in preparation to MAST-U operation". In: *Fusion Engineering and Design* 161 (2020), p. 111932. ISSN: 0920-3796. DOI: https://doi.org/10.1016/j.fusengdes.2020.111932. URL: https://www.sciencedirect.com/science/article/pii/S0920379620304804.

[2] T.C Hender et al. "Chapter 3: MHD stability, operational limits and disruptions". In: *Nuclear Fusion* 47.6 (June 2007), S128–S202. DOI: 10.1088/0029-5515/47/6/s03. URL: https://doi.org/10.1088/0029-5515/47/6/s03.

[3] D.F. Howell, T.C. Hender, and G. Cunningham. "Locked mode thresholds on the MAST spherical tokamak". In: *Nuclear Fusion* 47.9 (Aug. 2007), pp. 1336–1340. DOI: 10.1088/0029-5515/47/9/034. URL: https://doi.org/10.1088/0029-5515/47/9/034.

[14] W. J Hogan. "Inertial Fusion State of the Art—A Collection of Overview and Technical Papers from IFSA2003". In: *Nuclear Fusion* 44.12 (Dec. 2004). DOI: 10.1088/0029-5515/44/12/e01. URL: https://doi.org/10.1088/0029-5515/44/12/e01.

[15] D. J. Campbell. "The physics of the International Thermonuclear Experimental Reactor FEAT". In: *Physics of Plasmas* 8.5 (2001), pp. 2041–2049. DOI: 10.1063/1.1348334. URL: https://doi.org/10.1063/1.1348334.

[16] K. Ikeda. "Progress in the ITER Physics Basis". In: *Nuclear Fusion* 47.6 (June 2007). DOI: 10.1088/0029-5515/47/6/e01. URL: https://doi.org/10.1088/0029-5515/47/6/e01.

[17] J. G. Cordey D. R. Sweetman and T. S. Green and. "Heating and plasma interactions with beams of energetic neutral atoms". In: *Philosophical Transactions of the Royal Society of London. Series A, Mathematical and Physical Sciences* (Apr. 1981). DOI: 10.1098/rsta.1981.0087. URL: http://www.jstor.org/stable/36852.

[18] D. Stork. "Neutral beam heating and current drive systems". In: *Fusion Engineering and Design* 14.1 (1991). 16th Symposium on Fusion Technology, pp. 111–133. ISSN: 0920-3796. DOI: https://doi.org/10.1016/0920-3796(91)90238-L. URL: https://www.sciencedirect.com/science/article/pii/092037969190238L.

[19] D.Q. Hwang and J.R. Wilson. "Radio frequency wave applications in magnetic fusion devices". In: *Proceedings of the IEEE* 69.8 (1981), pp. 1030–1043. DOI: 10.1109/PROC.1981.12113.

[22] D.E. Post et al. "Steady-state radiative cooling rates for low-density, high-temperature plasmas". In: *Atomic Data and Nuclear Data Tables* 20.5 (1977), pp. 397–439. ISSN: 0092-640X. DOI: https://doi.org/10.1016/0092-640X(77)90026-2. URL: https://www.sciencedirect.com/science/article/pii/0092640X77900262.

[23] M. Bornatici et al. "Electron cyclotron emission and absorption in fusion plasmas". In: *Nuclear Fusion* 23.9 (Sept. 1983), pp. 1153–1257. DOI: 10.1088/0029-5515/23/9/005. URL: https://doi.org/10.1088/0029-5515/23/9/005.

[24] J. Winter. "A comparison of tokamak operation with metallic getters (Ti, Cr, Be) and boronization". In: *Journal of Nuclear Materials* 176-177 (1990), pp. 14–31. ISSN: 0022-3115. DOI: https://doi.org/10.1016/0022-3115(90)90025-I. URL: https://www.sciencedirect.com/science/article/pii/002231159090025I.

[25] Robert J Goldston. "Energy confinement scaling in Tokamaks: some implications of recent experiments with Ohmic and strong auxiliary heating". In: *Plasma Physics and Controlled Fusion* 26.1A (Jan. 1984), pp. 87–103. DOI: 10.1088/0741-3335/26/1a/308. URL: https://doi.org/10.1088/0741-3335/26/1a/308.

[26] J.W. Connor and J.B. Taylor. "Scaling laws for plasma confinement". In: *Nuclear Fusion* 17.5 (Oct. 1977), pp. 1047–1055. DOI: 10.1088/0029-5515/17/5/015. URL: https://doi.org/10.1088/0029-5515/17/5/015.

[27] K. M. McGuire et al. "Review of deuterium–tritium results from the Tokamak Fusion Test Reactor". In: *Physics of Plasmas* 2.6 (1995), pp. 2176–2188. DOI: 10.1063/1.871303. eprint: https://doi.org/10.1063/1.871303. URL: https://doi.org/10.1063/1.871303.

[28] Sergio Ciattaglia et al. "Energy Analysis for the Connection of the Nuclear Reactor DEMO to the European Electrical Grid". In: *Energies* 13.9 (2020). ISSN: 1996-1073. DOI: 10.3390/en13092157. URL: https://www.mdpi.com/1996-1073/13/9/2157.

[29] V.D. Shafranov. "Stellarators". In: *Nuclear Fusion* 20.9 (Sept. 1980), pp. 1075–1083. DOI: 10.1088/0029-5515/20/9/005. URL: https://doi.org/10.1088/0029-5515/20/9/005.

[30] H.A.B. Bodin. "The reversed field pinch". In: *Nuclear Fusion* 30.9 (Sept. 1990), pp. 1717–1737. DOI: 10.1088/0029-5515/30/9/005. URL: https://doi.org/10.1088/0029-5515/30/9/005.

[31] V E Golant. "Plasma penetration near the lower hybrid frequency." In: *Soviet Physics Technical Physics* (Jan. 1972). URL: https://www.osti.gov/biblio/4652568.

[33] S. Bernabei et al. "Lower-Hybrid Current Drive in the PLT Tokamak". In: *Phys. Rev. Lett.* 49 (17 Oct. 1982), pp. 1255–1258. DOI: 10.1103/PhysRevLett.49.1255. URL: https://link.aps.org/doi/10.1103/PhysRevLett.49.1255.

[34] R. Hagemann, G. Nief, and E. Roth. "Absolute isotopic scale for deuterium analysis of natural waters. Absolute D/H ratio for SMOW1". In: *Tellus* 22.6 (1970), pp. 712–715. DOI: https://doi.org/10.1111/j.2153-3490.1970.tb00540.x. URL: https://onlinelibrary.wiley.com/doi/abs/10.1111/j.2153-3490.1970.tb00540.x.

[35] Ernest E. Angino and Gale K. Billings. "Lithium content of sea water by atomic absorption spectrometry". In: *Geochimica et Cosmochimica Acta* 30.2 (1966), pp. 153–158. ISSN: 0016-7037. DOI: https://doi.org/10.1016/0016-7037(66)90104-9. URL: https://www.sciencedirect.com/science/article/pii/0016703766901049.

[36] T. Hino and M. Akiba. "Japanese developments of fusion reactor plasma facing components". In: *Fusion Engineering and Design* 49-50 (2000), pp. 97–105. ISSN: 0920-3796. DOI: https://doi.org/10.1016/S0920-3796(00)00349-5. URL: https://www.sciencedirect.com/science/article/pii/S0920379600003495.

[37] H Bolt et al. "Materials for the plasma-facing components of fusion reactors". In: *Journal of Nuclear Materials* 329-333 (2004). Proceedings of the 11th International Conference on Fusion Reactor Materials (ICFRM-11), pp. 66–73. ISSN: 0022-3115. DOI: https://doi.org/10.1016/j.jnucmat.2004.04.005. URL: https://www.sciencedirect.com/science/article/pii/S0022311504001242.

[38] J.A. Wesson. "Hydromagnetic stability of tokamaks". In: *Nuclear Fusion* 18.1 (Jan. 1978), pp. 87–132. DOI: 10.1088/0029-5515/18/1/010. URL: https://doi.org/10.1088/0029-5515/18/1/010.

[40] H. P. Furth, P. H. Rutherford, and H. Selberg. "Tearing mode in the cylindrical tokamak". In: *The Physics of Fluids* 16.7 (1973), pp. 1054–1063. DOI: 10.1063/1.1694467. URL: https://aip.scitation.org/doi/abs/10.1063/1.1694467.

[41] J.T Scoville and R.J. La Haye. "Multi-mode error field correction on the DIII-D tokamak". In: *Nuclear Fusion* 43.4 (Mar. 2003), pp. 250–257. DOI: 10.1088/0029-5515/43/4/305. URL: https://doi.org/10.1088/0029-5515/43/4/305.

[42] A. Kirk et al. "Measurement, correction and implications of the intrinsic error fields on MAST". In: *Plasma Physics and Controlled Fusion* 56.10 (Aug. 2014), p. 104003. DOI: 10.1088/0741-3335/56/10/104003. URL: https://doi.org/10.1088/0741-3335/56/10/104003.

[43] E.J. Strait et al. "Measurement of tokamak error fields using plasma response and its applicability to ITER". In: *Nuclear Fusion* 54.7 (Apr. 2014), p. 073004. DOI: 10.1088/0029-5515/54/7/073004. URL: https://doi.org/10.1088/0029-5515/54/7/073004.

[44] M. Greenwald et al. "A new look at density limits in tokamaks". In: *Nuclear Fusion* 28.12 (Dec. 1988), pp. 2199–2207. DOI: 10.1088/0029-5515/28/12/009. URL: https://doi.org/10.1088/0029-5515/28/12/009.

[51] R.J Buttery et al. "Error field mode studies on JET, COMPASS-D and DIII-D, and implications for ITER". In: *Nuclear Fusion* 39.11Y (Nov. 1999), pp. 1827–1835. DOI: 10.1088/0029-5515/39/11y/323. URL: https://doi.org/10.1088/0029-5515/39/11y/323.

[52] R. J. La Haye and J. T. Scoville. "A method to measure poloidal field coil irregularities in toroidal plasma devices". In: *Review of Scientific Instruments* 62.9 (1991), pp. 2146–2153. DOI: 10.1063/1.1142330. URL: https://doi.org/10.1063/1.1142330.

[53] Y. Q. Liu et al. "Feedback stabilization of nonaxisymmetric resistive wall modes in tokamaks. I. Electromagnetic model". In: *Physics of Plasmas* 7.9 (2000), pp. 3681–3690. DOI: 10.1063/1.1287744. URL: https://doi.org/10.1063/1.1287744.

[54] Marku Rampp et al. "GPEC: A Real-Time–Capable Tokamak Equilibrium Code". In: *Fusion Science and Technology* 70.1 (2016), pp. 1–13. DOI: 10.13182/FST15-154. URL: https://doi.org/10.13182/FST15-154.

Books

[4] L.A. Artsimovich et al. *Controlled Thermonuclear Reactions*. Plasma physics and laboratory astrophysics. Gordon and Breach Science Publishers, 1964. ISBN: 9780677200200. URL: https://books.google.it/books?id=AunRcbC8V0QC.

[5] S. Glasstone et al. *Controlled Thermonuclear Reactions: An Introduction to Theory and Experiment*. Van Nostrand, 1960. URL: https://books.google.it/books?id=fO9N3LypCYcC.

[6] R.A. Gross. *Fusion Energy*. A Wiley-interscience publication. Wiley, 1984. ISBN: 9780471884705. URL: https://books.google.it/books?id=3HZTAAAAMAAJ.

[7] A.R. Choudhuri and P.P.A.R. Choudhuri. *The Physics of Fluids and Plasmas: An Introduction for Astrophysicists*. Cambridge University Press, 1998. ISBN: 9780521555432. URL: https://books.google.it/books?id=i%5C_kufpYwkpQC.

[8] T. Kammash. *Fusion Reactor Physics: Principles and Technology*. Ann Arbor Science, 1975. ISBN: 9780250400768. URL: https://books.google.it/books?id=uROOAAAAIAAJ.

[9] R.D. Gill. *Plasma Physics and Nuclear Fusion Research*. Elsevier Science, 2013. ISBN: 9781483217932. URL: https://books.google.it/books?id=5rg3BQAAQBAJ.

[10] J. Wesson and D.J. Campbell. *Tokamaks*. International Series of Monographs on Physics. OUP Oxford, 2011. ISBN: 9780199592234. URL: https://books.google.it/books?id=XJssMXjHUr0C.

[11] D.J. Rose and M. Clark. *Plasmas and Controlled Fusion: By David J. Rose and Melville Clark, Jr.* M.I.T. Press, 1961. URL: https://books.google.it/books?id=KL5EAAAAIAAJ.

[12] G.H. Miley, N. Ivich, and H.H. Towner. *Fusion Cross Sections and Reactivities*. Report COO-2218-17. University of Illinois, C-U Campus, Nuclear Engineering Program, 1974. URL: https://books.google.it/books?id=B09oYgEACAAJ.

[13] K. Miyamoto. *Plasma Physics for Nuclear Fusion*. MIT Press, 1989. ISBN: 9780262132374. URL: https://books.google.it/books?id=mwRBAQAAIAAJ.

[20] R.J. Goldston. *Introduction to Plasma Physics*. CRC Press, 2020. ISBN: 9781439822074. URL: https://books.google.it/books?id=7kM7yEFUGnAC.

[21] W.H. Tucker. *Radiation Processes in Astrophysics*. Cambridge, 1975. ISBN: 9780262200219. URL: https://books.google.it/books?id=FR81AQAAIAAJ.

[32] T.H. Stix. *The Theory of Plasma Waves*. McGraw-Hill advanced physics monograph series. McGraw-Hill, 1962. URL: https://books.google.it/books?id=eZ48AAAAIAAJ.

[39] Jeffrey P Freidberg. *Plasma physics and fusion energy*. Cambridge university press, 2008. DOI: doi:10.1017/CBO9780511755705.

[45] B. Girod, R. Rabenstein, and A. Stenger. *Signals and Systems*. Wiley, 2001. ISBN: 9780471988007. DOI: https://doi.org/10.1007/978-3-642-01359-1_2.

Websites

[46] *System Identification Toolbox Documentation - MathWorks*. URL: https://it.mathworks.com/help/ident/.

[47] *MATLAB tfest - Estimate transfer function - MathWorks*. URL: https://it.mathworks.com/help/ident/ref/tfest.html.

[48] *MATLAB lsim Simulated response data - MathWorks*. URL: https://it.mathworks.com/help/control/ref/lti.lsim.html.

[49] *Simple moving average filtering*. URL: https://en.wikipedia.org/wiki/Moving_average.

[50] *EUROFusion Reseach Topic 1*. URL: https://wiki.euro-fusion.org/wiki/WPTE_wikipages:_Experimental_campaign_2021:RT01.